International Journal of Pharmaceutics: X 6 (2023) 100215

Contents lists available at ScienceDirect

International Journal of Pharmaceutics: X

journal homepage: www.sciencedirect.com/journal/international-journal-of-pharmaceutics-x

Enhancing the anticancer potential of metformin: fabrication of efficient nanospanlastics, *in vitro* cytotoxic studies on HEP-2 cells and reactome enhanced pathway analysis

Shereen Nader Raafat [a,b], Sara Abd El Wahed [c], Noha M. Badawi [d,e], Mona M. Saber [f,**], Maha R.A. Abdollah [e,g,*]

[a] Department of Pharmacology, Faculty of Dentistry, The British University in Egypt, Cairo, Egypt
[b] Stem Cells and Tissue Culture Hub (CIDS), Faculty of Dentistry, The British University in Egypt, Cairo, Egypt
[c] Department of Oral Pathology, Faculty of Dentistry, The British University in Egypt, Cairo, Egypt
[d] Department of Pharmaceutics and Pharmaceutical Technology, Faculty of Pharmacy, The British University in Egypt, Cairo, Egypt
[e] Center for Drug Research and Development (CDRD), Faculty of Pharmacy, The British University in Egypt, El Sherouk City, Egypt
[f] Department of Pharmacology and Toxicology, Faculty of Pharmacy, Cairo University, Giza, Egypt
[g] Department of Pharmacology, Faculty of Pharmacy, The British University in Egypt, Cairo, Egypt

ARTICLE INFO

Keywords:
Metformin
Spanlastics
Nanovesicles
HEP-2 cells
Reactome analysis

ABSTRACT

Metformin (MET), an oral antidiabetic drug, was reported to possess promising anticancer effects. We hypothesized that MET encapsulation in unique nanospanlastics would enhance its anticancer potential against HEP-2 cells. Our results showed the successful fabrication of Nano-MET spanlastics (d = 232.10 ± 0.20 nm; PDI = 0.25 ± 0.11; zeta potential = (−) 44.50 ± 0.96; drug content = 99.90 ± 0.11 and entrapment efficiency = 88.01 ± 2.50%). MTT assay revealed the enhanced Nano-MET cytotoxicity over MET with a calculated IC_{50} of 50 µg/mL and > 500 µg/mL, respectively. Annexin *V*/PI apoptosis assay showed that Nano-MET significantly decreased the percentage of live cells from 95.49 to 93.70 compared to MET and increased the percentage of cells arrested in the G0/G1 phase by 8.38%. Moreover, Nano-MET downregulated BCL-2 and upregulated BAX protein levels by 1.57 and 1.88 folds, respectively. RT-qPCR revealed that Nano-MET caused a significant 13.75, 4.15, and 2.23-fold increase in caspase-3, −8, and − 9 levels as well as a 100 and 43.47-fold decrease in cyclin D1 and mTOR levels, respectively. The proliferation marker Ki67 immunofluorescent staining revealed a 3-fold decrease in positive cells in Nano-MET compared to the control. Utilizing the combined Pathway-Enrichment Analysis (PEA) and Reactome analysis indicated high enrichment of certain pathways including nucleotides metabolism, Nudix-type hydrolase enzymes, carbon dioxide hydration, hemostasis, and the innate immune system. In summary, our results confirm MET cytotoxicity enhancement by its encapsulation in nanospanlastics. We also highlight, using PEA, that MET can modulate multiple pathways implicated in carcinogenesis.

1. Introduction

Drug repurposing is the process of finding new therapeutic uses for already approved or investigational drugs beyond the scope of their original medical indication (Pushpakom et al., 2019). It offers numerous advantages including low risk of failure, reduction in the drug development time frame, significantly lower costs, and known safety profiles of the repurposed drugs (Pushpakom et al., 2019). Drug repurposing is particularly encouraged in diseases where conventional therapies fail to accomplish the promised therapeutic outcomes to fulfill the ever-growing clinical needs. Of these diseases, cancer is one of the top priorities as it is a major health concern and the second leading cause of death worldwide (Yu et al., 2019). Surgical resection, radiation, and chemotherapy are the standard of care for the treatment of cancer, nonetheless, emergence of resistance remains a challenge (Yu et al., 2019).

* Correspondence to: M.R.A. Abdollah, Department of Pharmacology, Faculty of Pharmacy, The British University in Egypt, El Sherouk City, Suez Desert Road, Cairo 11837, Egypt.
** Correspondence to: M.M. Saber, Department of Pharmacology and Toxicology, Faculty of Pharmacy, Cairo University, Giza, Kasr El-Aini 11562, Egypt.
E-mail addresses: mona.magdy@pharma.cu.edu.eg (M.M. Saber), maha.abdollah@bue.edu.eg (M.R.A. Abdollah).

https://doi.org/10.1016/j.ijpx.2023.100215
Received 14 May 2023; Received in revised form 17 October 2023; Accepted 21 October 2023
Available online 23 October 2023

Most of the diagnosed head and neck malignancies, known as head and neck squamous cell carcinoma (HNSCC), originate from the mucosal epithelium of the oral cavity, pharynx, and larynx (Johnson et al., 2020). This aggressive tumor has a fatal prognosis despite the use of numerous treatment protocols (Rego et al., 2017). One of the most prevalent HNSCC is laryngeal squamous cell carcinoma (LSCC) with an estimated 184,615 newly diagnosed cases and mortalities of 99,840 patients in 2020 (Missale et al., 2023). Usually, stage I tumors have the most favorable prognosis, unlike advanced stage LSCC which has a very low survival rate (Missale et al., 2023). The five-year rate of survival has decreased from 66% to 63% over the past 40 years. In the ongoing fight against head and neck malignancies, greater emphasis is now being placed on developing novel therapeutic strategies (Heng et al., 2023).

Metformin (MET), an oral hypoglycemic drug that is considered the first-line therapy for type 2 diabetes mellitus (Sanchez-Rangel and Inzucchi, 2017), represents an exciting candidate for drug repurposing owing to its efficacy, safety, and affordability. The anticancer potential of MET has been extensively studied and it was shown to limit cancer cell growth in multiple cancer types, including gastric, pancreatic, uterine, prostate, colon, and breast cancers (Ugwueze et al., 2020). MET inhibits protein synthesis and cell proliferation by activating various proteins, e.g., adenosine monophosphate-activated kinase (AMPK), enzymes ataxia telangiectasia mutated (ATM) and liver kinase B1 (LKB1) (Ke et al., 2018; Tawfik et al., 2022). Of great interest is the enhancement of AMPK activity, which is an enzyme responsible for cellular energy regulation and change in the ATP: AMP ratio. AMPK stimulates other additional essential processes such as glucose uptake, glycolysis, beta-oxidation of fatty acids, and mitochondrial biogenesis, while it inhibits other pathways to reserve ATP such as protein, sterol, and glycogen synthesis (Ke et al., 2018). AMPK activation also reduces mTOR action and activates P53, resulting in autophagy and apoptosis (Krishan et al., 2015). The lowering of insulin and insulin-like growth factors, the blocking of endogenous reactive oxygen species (ROS), and the suppression of chronic inflammation are all hypothesized as additional AMPK-independent possibilities for its anticancer activity (Saraei et al., 2019; Ugwueze et al., 2020).

Despite the promising results obtained with MET, targeted drug delivery remains one of the main challenges hindering the development of safe and well tolerated anticancer therapies. New medication delivery methods based on nanotechnology are being used to improve the efficacy of cancer therapy while decreasing adverse effects (Calixto et al., 2014; Hashemzadeh et al., 2021; Vahidfar et al., 2021). By encapsulating medications in non-toxic and biodegradable nano delivery systems, multiple advantages could be achieved. For instance, less side effects, longer half-life in the bloodstream, enhanced medication pharmacokinetics, and more patient compliance (Calixto et al., 2014).

One of the most promising and exciting new nanoformulations currently being investigated is spanlastics. They offer many advantages such as enhanced therapeutic efficacy, improved drug bioavailability and less toxic side effects of the formulated drug (Ansari et al., 2022). Spanlastics are surfactant-based nanovesicles consisting of a non-ionic surfactant and an edge activator (Badria and Mazyed, 2020). Spanlastics are biodegradable systems that possess many unique properties such as: elasticity, deformability, non-immunogenicity, minimum toxicity and compatibility with the biological membranes owing to the presence of non-ionic surfactants (Sharma et al., 2020). The elastic nature of spanlastics is particularly advantageous as they are capable of squeezing themselves through the biological membranes without causing disruption or being disrupted themselves (Mazyed et al., 2021).

Recently, considerable studies have adopted various powerful methods to forecast adverse reactions, clarify dangerous toxicity problems, and reveal drug resistance mechanisms for a wide range of therapeutics (Bezerianos et al., 2017). Among these high-throughput methods, pathway-enrichment analysis (PEA), Reactome-mining, and their combination (PEA-Reactome mining) have proved their effectiveness in providing mechanistic insight of high-throughput omics data aided with interactive visualization, interpretation, and mapping of pathway knowledge at the systems biology level (Cheng et al., 2009). Reactome maps illustrate how different biological entities such as nucleic acids, proteins, complexes, and other molecules are included in multiple biological pathways such as metabolism, signaling, adapted and innate immunity, apoptosis, transcriptional regulation, and various diseases (Kao et al., 2017). Therefore, utilizing the PEA-Reactome approach could help identify and test candidate drugs for treating various cancers in the pharmaco-genomic analysis context and correlate with drug sensitivity (Cheng et al., 2009; Haider et al., 2018).

Given the benefits of MET as a safe and well-tolerated oral antidiabetic agent, it represents an exciting candidate for repurposing as an anticancer agent. The aim of the current study was to evaluate the hypothesis that the encapsulation of MET in nanospanlastics will enhance its anticancer potential against HEP-2 laryngeal cancer cells. We tested our hypothesis using several functional assays and further evaluated the molecular markers implicated in the enhanced cytotoxicity of MET nanospanlastics. In addition, we performed an in-depth PEA-Reactome analysis for MET to understand the pathways that the drug targets and the molecular complexities of each pathway.

2. Materials and methods

2.1. Materials

Human HEP-2 cell line was purchased from Nawah Scientific (Cairo, Egypt). MET was a kind gift from Nile Pharmaceuticals and Chemical Industries (Cairo, Egypt). Fetal bovine serum (FBS) and Dulbecco's modified Eagle's medium (DMEM) were purchased from Gibco®, Thermo Fisher Scientific, USA. The antibiotic-antimycotic mixture consisting of 100 U/mL of penicillin, 0.1 U/mL streptomycin and 0.25 μg/mL of Amphotericin B was obtained from Lonza®, USA. Transcutol® P was a kind gift from Gattefossé, France. Ethanol was bought from Fisher Scientific (UK). Span 60 and dialysis tubing cellulose membrane, with molecular weight cut off of 12,000–14,000 Da, were obtained from Sigma-Aldrich (St Louis, MO, USA).

2.2. Methods

2.2.1. Preparation of MET-loaded nanospanlastics (Nano-MET)

MET-loaded nanospanlastics (Nano-MET) were formulated by using the ethanol injection method (Fahmy et al., 2018). Two nanospanlastics formulations were prepared: S1 and S2. Each formulation contained Span® 60 as well as Tween® 80 as an edge activator (EA) with or without Transcutol® P as a penetration enhancer. S1: 300 mg Span® 60 and 100 mg of Tween® 80 (3:1 weight ratio) and S2: 300 mg of Span® 60, 100 mg of Tween® 80, and 100 mg Transcutol® P (3:1:1 weight ratio). The encapsulation process started by dissolving the drug (MET) along with Span 60 in 2 mL ethanol and the mixture was injected drop-by-drop into a hot (60 °C) Tween® 80 solution with or without Transcutol® P (in deionized water). Each formulation contained 10 mg of MET, with a total volume of 10 mL. The hydroalcoholic solution that resulted was constantly stirred for 30 min at 800 rpm on a magnetic stirrer to completely evaporate any remaining ethanol and form Nano-MET dispersions. Subsequently, sonication was performed using an ultrasonic water bath (Crest ultrasonics Corp., Trenton, NJ, USA) for 5 min to acquire a suitable particle size. Nano-MET dispersions were washed twice by centrifugation at 12,000 rpm for 2 h with deionized water to eliminate the unentrapped drug from the nanoparticles surface. Nanoparticles were then re-dispersed in the same volume of the deionized water. The vesicular dispersions were stored at 4 °C until further investigation. Composition of the prepared nanovesicles is displayed in Table 1.

Table 1
Composition of the prepared nanospanlastics loaded with MET.

Formulae Code	Span 60 (mg)	Tween 80 (mg)	Transcutol® P (mg)
S1	300	100	–
S2	300	100	100

2.2.2. Characterization of the prepared Nano-MET

2.2.2.1. Particle size (PS), Polydispersity index (PDI), and Zeta potential (ZP) measurement. The prepared formulations' PS, PDI, and ZP were measured using a Malvern Zetasizer (Malvern Instruments Ltd., UK) using the dynamic light scattering technique at 25 °C after proper dilution using deionized water (Shaaban et al., 2019).

2.2.2.2. Drug content (DC) and Entrapment efficiency percent (EE%). Methanol was utilized to breakdown the nanovesicles and release the drug (Fahmy et al., 2018). The whole DC (unentrapped + entrapped) of the fabricated formulae was assessed by dissolving 1 mL of nanospanlastics dispersion in 25 mL methanol and then measuring the U*V* absorbance *via* UV–Vis spectrophotometer (V-630, Jasco, Tokyo, Japan) at λ_{max} 233 nm (Mokale et al., 2016). The EE% was determined by the centrifugation method. Nanovesicles were centrifuged for 2 h (h) at 12000 rpm at 4 °C, the clear supernatant was withdrawn and the absorbance was measured at λ_{max} 233 nm (Mokale et al., 2016) in order to assess the amount of free drug spectrophotometrically. The following equation was employed to calculate the EE% (Badawi et al., 2022).

$$EE\% = \left(\frac{\text{Total MET concentration} - \text{Free MET concentration}}{\text{Total MET concentration}}\right) \text{x } 100$$

2.2.2.3. Transmission electron microscopy. Transmission electron microscopy (TEM) (Jeol JEM1230, Tokyo, Japan) was used to examine the morphological appearance of the selected Nano-MET after proper dilution. Before TEM observation, one drop of the chosen formulation was applied to a copper grid and allowed to air dry for 10 min at room temperature. (Elsherif et al., 2017).

2.2.2.4. Fourier transform infrared (FTIR) spectroscopy. Using the FTIR spectrophotometer VERTEX 70 (Bruker Corporation, Germany), infrared spectra of the pure drug MET, medicated selected formula, and plain formula (without drug) were obtained (Eissa et al., 2021). The spectra were examined in the range of 500 to 4000 cm^{-1}. Before analyzing each sample, the spectrum of air was utilized as a background. Sample spectra and the background were collected at 22–24 °C and spectral resolution of 4 cm^{-1}. For each assessment, 32 scans were performed.

2.2.2.5. In vitro dissolution studies. The *in vitro* drug release of MET from the selected formulation was assessed through the dialysis bag technique and compared with free MET in order to show the change in the release profile of the drug following encapsulation into the nanospanlastics (Badawi et al., 2022; Mazyed et al., 2021). Firstly, the cellulose dialysis bag was presoaked in distilled water for 12 h. Next, nanospanlastics dispersion equivalent to 1 mg of MET were weighed and an equal amount of free MET was resuspended in phosphate buffer solution (PBS) at pH 7.4 and then vortexed for 2 min. The solutions were placed in the presoaked dialysis bag and the ends were firmly tied before being immersed in 50 mL PBS at pH 7.4 (mimicking the receptor cell at physiological conditions) (Badawi et al., 2022; Mazyed et al., 2021) in a shaking water bath at 37 ± 0.5 °C and 100 rpm. At time intervals ranging from 1 to 24 h, aliquots were taken from each receptor cell and substituted with equivalent volumes of fresh release medium. Samples were then spectrophotometrically analyzed against PBS as a blank at λ_{max} 233 nm (Mokale et al., 2016). The average concentration was determined after measuring the samples three times.

2.2.3. Cell culture

HEP-2 cells were cultured to 80% confluency in a humidified incubator at 37 °C and 5% CO_2 in DMEM high glucose medium supplemented with 10% FBS and 1% antibiotic/antimycotic mixture. HEP-2 cells were tested for mycoplasma contamination and were found to be negative. All cell culture procedures were conducted inside a class II laminar flow hood and incubations were done at 37 °C inside the incubator, unless otherwise specified.

2.2.4. Cancer cytotoxicity, hemocompatibility and cellular uptake of nanospanlastics

Using the MTT (3-[4,5-dimethylthiazol-2-yl]-2,5 diphenyl tetrazolium bromide) test, the cytotoxicity of MET and Nano-MET on HEP-2 cancer cells was evaluated. In a 96-well plate, 10^4 cells were seeded in 0.2 mL of medium per well and left overnight to attached inside the incubator. Next day, cells were treated with serial dilutions of MET and Nano-MET formulation (500 µg/mL - 3.9 µg/mL). After 72 h, the culture medium was substituted with 100 µL/well of 5 mg/mL MTT solution prepared in fresh DMEM medium. The cells were incubated for 2 h before the supernatant was removed and replaced with 100 µL/well of DMSO to dissolve the formed formazan crystals. At wavelength of 570 nm, absorbance was determined using a microplate reader (Thermo Scientific Multiscan GO, USA). Subsequently, the 50% inhibitory concentrations (IC_{50}) of the treatments were obtained using the non-linear regression analysis (Abdollah et al., 2023) *via* GraphPad Prism software.

To assess the Nano-MET formulation hemocompatibility *in vitro*, erythrocytes hemolysis assay (Mazzarino et al., 2015) was performed using three different concentrations of nanospanlastics including the IC_{50} (50 µg/mL) as well as 25 µg/mL and 100 µg/mL (see Supplementary data A.1 for full details).

For the determination of Nano-MET cellular uptake, HEP-2 cells were incubated with 50 µg/mL of Nano-MET for 72 h. Cells were washed twice to remove uninternalized nanospanlastics, cells were then fixed using 3% glutaraldehyde for 3 h followed by staining with osmium tetroxide for transmission electron microscope (TEM) imaging. The samples were dehydrated using increasing concentrations of ethanol then infiltrated with increasing concentrations of embedding resin. All samples were put in an oven to ensure resin complete polymerization, then trimmed and mounted on a microtome to slice the samples into 50–70 nm thick sections and then placed on carbon-coated copper grid for TEM imaging (Talos™ F200i TEM, Thermo Scientific, USA) using 200 k*V*.

2.2.5. Annexin V/ propidium iodide (PI) apoptosis assay and cell cycle analysis

For both the detection of apoptosis and the study of the cell cycle progression following drug treatments, 2×10^6 cells were seeded in T-75 flasks and allowed to adhere overnight. The next day, cells were treated for 72 h with MET and Nano-MET at 50 µg/mL. Fresh medium served as the control. The treated cells were collected by the addition of trypsin followed by washing twice with cold PBS by centrifugation at 280 x*g* for 5 min. The pellet was then resuspended in cold PBS and kept on ice until analysis by flow cytometry technique.

For the apoptosis assay, 100 µL of the cell suspension of each sample was incubated for 15 min in the dark with 5 µL of Annexin V-FITC and 1 µL of PI stock (100 µg/mL). Each sample was then treated with 400 µL of 1× Annexin binding buffer and analyzed on a CytoFlex flow cytometer (Beckman Coulter, CA, USA) as per the manufacturer's guidelines. A minimum of 10,000 events were recorded, and data was analyzed using CytExpert software (Beckman Coulter, CA, USA).

For the analysis of cell cycle progression, cells were fixed by resuspending the pellets in 2 mL solution of 60% ice-cold ethanol for 1 h at 4 °C followed by washing twice with PBS. Cells were then resuspended in 1 mL nucleic acid staining mixture (10 µg/mL PI and 50 µg/mL RNAase A in PBS) for 20 min in the dark at 37 °C. Cell cycle distribution was calculated using CytExpert software (Beckman Coulter, CA, USA) and at least 10,000 events were acquired.

Table 2
Sequence of the primers used in RT-qPCR experiments.

Genes	Sequence
BAX	Forward CAAGAAGCTGAGCGAGTGTCT Reverse CAGTTGAAGTTGCCGTCAGA
BCL-2	Forward GATTGTGGCCTTCTTTGAG Reverse CAAACTGAGCAGAGTCTTC
Caspase-3	Forward TCGGTCTGGTACAGATGTCG Reverse GGCTCAGAAGCACACAAACA
Caspase-8	Forward CATAGAGATGGAGAAGAGGGTCA Reverse GGACTTCCTTCAAGGCTGCT
Caspase-9	Forward AAAATGGTGCTGGCTTTGCT Reverse CACAATCTTCTCGACCGACAC
Cyclin D1	Forward TGGTGAACAAGCTCAAGTGG Reverse ATGGAGGGCGGATTGGAAAT
mTOR	Forward CCCTACTTTGCTTGAGGTGC Reverse TGGATTCTGACAGGCTGACA
β-actin	Forward AGCACAGAGCCTCGCCTTT Reverse CACGATGGAGGGGAAGAC

2.2.6. Quantitative analysis of apoptosis and proliferation related markers using real time quantitative polymerase chain rection (RT-qPCR)

Apoptosis-related markers BAX, BCL-2, caspase-3, caspase-8 and caspase-9 together with cell cycle and proliferation regulatory protein cyclin D and mammalian target of rapamycin (mTOR) were determined using RT-qPCR. Briefly, cells (7×10^5) were seeded in triplicates into T-25 flasks and treated with MET and Nano-MET at 50 μg/mL for 72 h. Cells incubated with normal culture medium served as the control group. Cells were then harvested, and RNA extraction was performed on cell pellets using a QIAGEN RNA extraction kit (QIAGEN, Hilden, Germany) as per the manufacturer's procedures. Reverse transcription and complementary DNA (cDNA) synthesis was then performed using RevertAid First Strand cDNA Synthesis Kit (Thermoscientific, MA, USA). Finally, amplification and quantification of cDNA were performed using SYBR Green Supermix (Bio-Rad) on an RT-qPCR system (Bio-Rad). The expression of mRNA was normalized against β-actin as a reference housekeeping gene. Analysis of data was performed using the ($2^{-\Delta\Delta ct}$) method. All samples were measured in triplicates ($n = 3$), and the experiment was repeated three times. Results are expressed as fold change relative to the control (Alhazmi et al., 2023; Saber et al., 2023). The sequence of the primers used are listed in Table 2.

2.2.7. Analysis of BAX and BCL-2 proteins by Western blotting

Briefly, 2×10^6 cells were seeded in triplicates into T-75 flasks and left to adhere overnight before being treated for 72 h with MET and Nano-MET at 50 μg/mL. Next, cells were harvested and treated with RIPA lysis buffer supplemented with a protease inhibitor (Thermo Scientific, USA,) as per the manufacturer's protocol. Total protein concentration was measured using the standard BCA protein assay (Thermo Scientific, USA) as per the manufacturer's protocol and samples were stored at −80 °C until further processing.

For Western blotting, 20 μg of purified protein was loaded per well onto an 8% SDS-PAGE gel and subsequently transferred to a PVDF membrane and blocked with 5% blocking buffer. Page Ruler Unstained Protein Ladder was used (cat no: 26614, Thermo Scientific, USA). The membrane was either probed with anti-BCL-2 antibody (cat no: PA5–27094, Thermo Scientific, USA), anti-BAX antibody (cat no: PA5–116541, Thermo Scientific, USA) or GAPDH antibody (Thermo Scientific, USA) which act as a loading control. The primary antibodies were used at a concentration of 1:500 and were incubated overnight on a shaking platform. Next day, the membranes were treated with the secondary antibody: goat anti-rabbit IgG (H + L), Biotin-XX (lot. no.1305936, Thermo Scientific, USA) and left overnight on a rocking platform. Then the substrate Qdot R 625 streptavidin conjugate (cat no. W10142, Thermo Scientific, USA) was further incubated with the membrane overnight on a rocking platform. Finally, the membrane was visualized at 340 nm using UVP Transilluminator gel documentation system (Analytik Jena, USA). The protein ratio was calculated as the ratio of protein concentration relative to that of the internal control protein (GAPDH) using the Analytica Jena software.

2.2.8. Immunofluorescence expression of Ki67

To determine the effects of Nano-MET and MET on HEP-2 cell proliferation, the cells were tested for Ki67 protein expression. Briefly, cells were treated for 72 h with MET and Nano-MET at 50 μg/mL before being fixed using warm 4% formaldehyde. Then, rabbit anti-Ki67 primary antibody (Invitrogen; Thermo Scientific, Hilden, Germany) was added to the fixed cells and incubated at 4 °C overnight. The cells were then washed with PBS followed by the addition of goat anti-rabbit IgG secondary antibody (Invitrogen; Thermo Scientific, Hilden; Germany). The slide was mounted with Prolong Gold Antifade Reagent (Abcam, Cambridge, UK) at room temperature overnight. Slides were imaged using a fluorescence microscope (LABOMED LX400, USA). To grade the strength of the immunofluorescence (IF) staining, a four-point scale was used as follows: 0 for no staining, 1 for faint staining, 2 for moderate staining, and 3 for severe staining (Turashvili et al., 2009). Each sample's H-score was determined by adding the intensity values (from 0 to 3) and the positive cell percentage (from 0% to 100%). The median value of H-score was calculated.

2.2.9. Target prediction, pathway enrichment analysis and reactome-mining

The Swiss Target Prediction online tool (http://www.swisstargetprediction.ch) was used to initially project all the biological targets for MET as an anticancer drug for target prediction analysis. The online DisGeNET hub (https://www.disgenet.org, accessed on 21 March 2023) was utilized to collect the available gene-disease association for laryngeal carcinoma. A Venn diagram was plotted using the InteractiVenn online toolbox (Heberle et al., 2015). Then, pathway enrichment analysis was done by the Cytoscape 3.8.2 toolbox to explore all potential target-functions relationships (Shannon et al., 2003). Finally, the fuzzy logic simulation model was employed to mimic Boolean-network dynamic behavior and generate a FoamTree graph based on the Voronoi tessellation analysis for MET's top predicted gene targets. This modeling, mapping, and visualization analysis was accomplished using the Cytoscape-based ReactomeFIViz software for all possible drug–target interactions (Blucher et al., 2019).

2.2.10. Statistical analysis

All statistical analyses were performed using GraphPad Prism software version 6.0. All results are presented as mean ± standard deviation (SD). Statistical analysis was done by One-way ANOVA followed by *post-hoc* Tukey's test. For all results, p-value <0.05 was considered significant. Each experiment was repeated at least 3 times with 3 to 6 replicates per treatment, representative data is shown.

Table 3
Characterization results of the prepared nanospanlastics loaded with MET.

Formulae code	PS (nm)	PDI	ZP (mV)	DC%	EE%
S1	264.90 ± 1.20	0.34 ± 0.02	(−) 36.40 ± 0.82	98.73 ± 0.33	85.03% ± 1.24
S2	232.10 ± 0.20	0.25 ± 0.11	(−) 44.50 ± 0.96	99.90 ± 0.11	88.01% ± 2.50

3. Results

3.1. Preparation and characterization of MET nanospanlastics

MET-loaded nanospanlastics were successfully fabricated by ethanol injection method. The formulae composition and the results of the characterization measurements are listed in Table 1 and Table 3, respectively.

The different formulae were evaluated using DLS to measure particle size (PS), polydispersity index (PDI) and zeta potential (ZP). The results (Table 3) showed that the nanospanlastics without Transcutol® P formulation (S1) exhibited a size of 264.90 ± 1.20 nm and PDI value of 0.34 ± 0.02. While, S2 formulation (with Transcutol® P) had a size of 232.10 ± 0.20 nm and PDI value of 0.25 ± 0.11. ZP was evaluated for S1 and S2 as it is crucial in understanding how the nanovesicles behave since charged vesicles resist fusion and aggregation unlike their uncharged counterparts (Elmowafy et al., 2019). The prepared nanospanlastics were all negatively charged, ranging from (−) 36.40 ± 0.82 mV to (−) 44.50 ± 0.96 mV (all exceeding (−) 30 mV) indicating their great stability.

As shown in Table 3, the drug content (DC%) measurements were 98.73 ± 0.33% and 99.90 ± 0.11% for S1 and S2, respectively, which were in the acceptable range. The ability of a nanocarrier to encapsulate drugs is one of its most important requirements, an ideal nanocarrier should load higher content of drugs (Barani et al., 2019). Entrapment efficiency percent (EE%) values for S1 and S2 were 85.03 ± 1.24% and 88.01 ± 2.50%, respectively, indicating the successful loading of MET into the nanovesicles in both formulations.

As per the abovementioned results, S2 formulation was selected for further investigation due to its smaller PS, PDI in addition to higher ZP and EE%. S2 will be referred to as Nano-MET in the next set of findings.

Morphological analysis done using Transmission Electron Microscopy (TEM) (Fig. 1) of the selected formula S2 (Nano-MET) showed smooth spherical shaped nanovesicles with relatively uniform size distribution. The size of the nanovesicles attained from TEM examination was in good harmony with the PS analysis.

The overlay Fourier transform infrared (FTIR) spectra of pure MET, void formula, and selected S2 formulation (Nano-MET) is shown in Fig. S1. MET characteristic bands are the amine N—H group at 3339, 3274 cm^{-1}, C—N, C═N at 1562, 1634 cm^{-1} wavenumbers, respectively, and the C—H bending at 1494 cm^{-1} (Salem et al., 2022). Span 60 spectra showed the O—H group at wave number 3410 cm^{-1}, alkanes, in addition to 1745 cm^{-1} (C═O stretch of ester), and aromatic rings at wavenumber 1449 cm^{-1} (Mekkawy et al., 2022; Salem et al., 2022). FTIR spectrum of Nano-MET showed that the characteristic absorption peaks of Span 60, while that of the MET disappeared indicating the drug encapsulation within the nanovesicles. In addition, the peaks of the S2 formula and the plain drug free formula were identical which confirms that MET was successfully encapsulated in the nanovesicles (Eissa et al., 2021).

The *in vitro* release of MET from the selected S2 nanospanlastics formulation compared to pure MET was measured in physiological release medium of phosphate buffered saline (PBS) (Fig. 2). The free MET exhibited a higher % of drug released which was 100 ± 0.02% after 1 h and this result confirm that the drug could diffuse easily through the dialysis membrane without being hindered, thus, the sink condition was successfully attained (Mazyed et al., 2021). In contrast, MET loaded into the nanospanlastics showed only 15.60 ± 0.70% after 1 h and demonstrated a controlled release profile reaching 80.80 ± 2.60% after 24 h.

3.2. Evaluation of cancer cytotoxicity, hemocompatibility and cellular uptake of nanospanlastics

To examine the effect of MET and Nano-MET formulation on HEP-2 cancer cell viability, cells were treated with serial dilutions of both treatments (500–3.9 μg/mL) for 72 h and cell viability was evaluated with MTT assay. Treatment of cells with MET did not cause any significant reduction in cell viability with the used drug concentrations (500–3.9 μg/mL). On the other hand, treatment with Nano-MET significantly reduced HEP-2 cell viability in a dose-dependent manner with a calculated IC_{50} value of 50 μg/mL (Fig. 3A). All subsequent assays in the present study were conducted using 50 μg/mL of both MET and

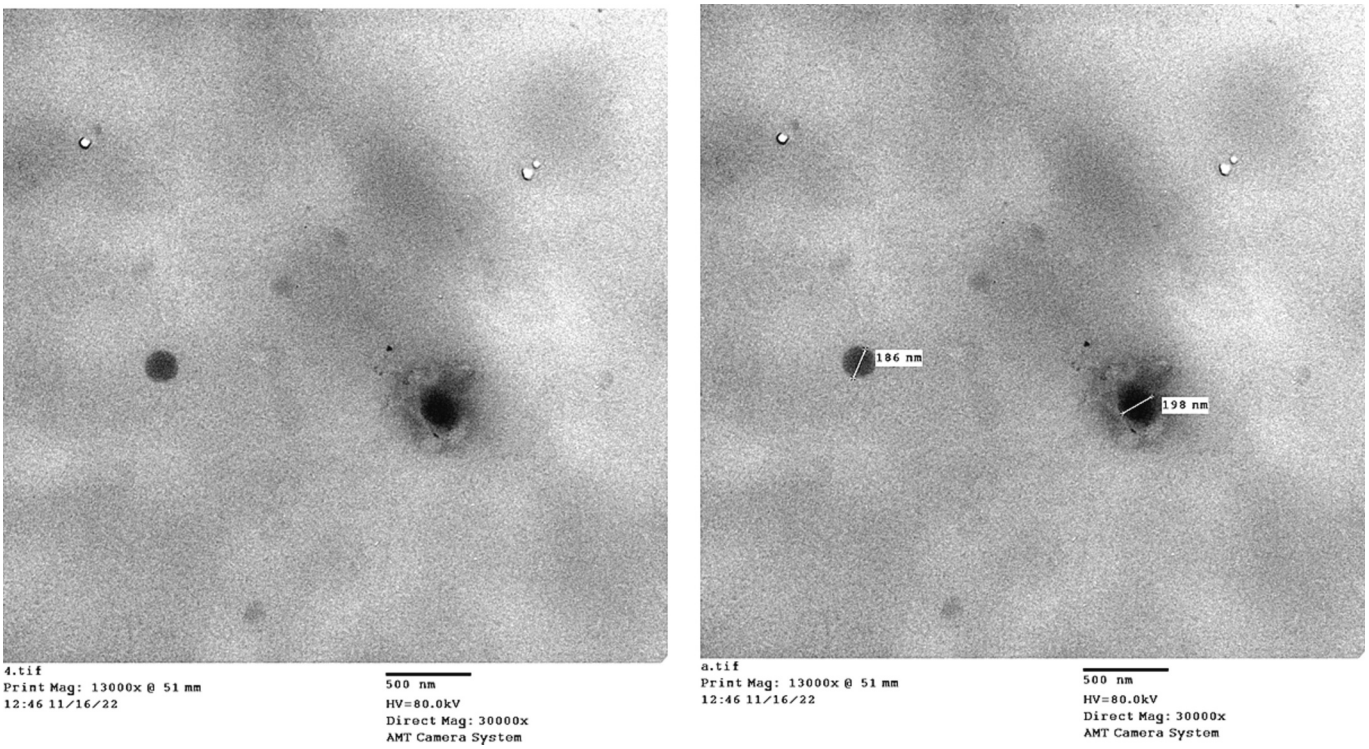

Fig. 1. Transmission electron microscopy (TEM) of the selected MET loaded spanlastics (S2, Nano-MET).

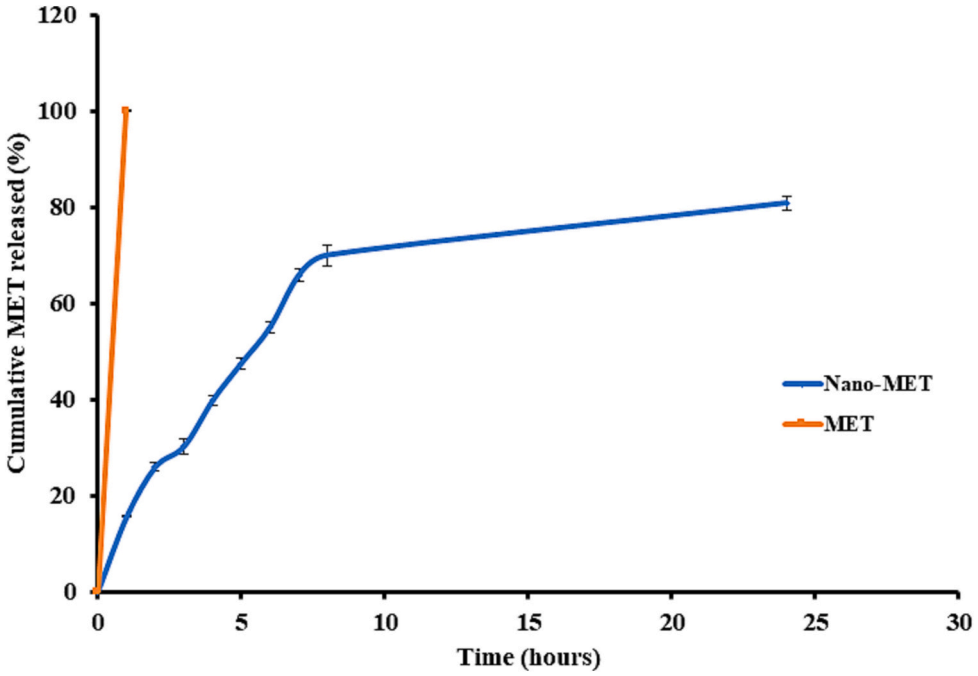

Fig. 2. *In vitro* drug release of the free MET and the selected MET loaded spanlastics (S2, Nano-MET).

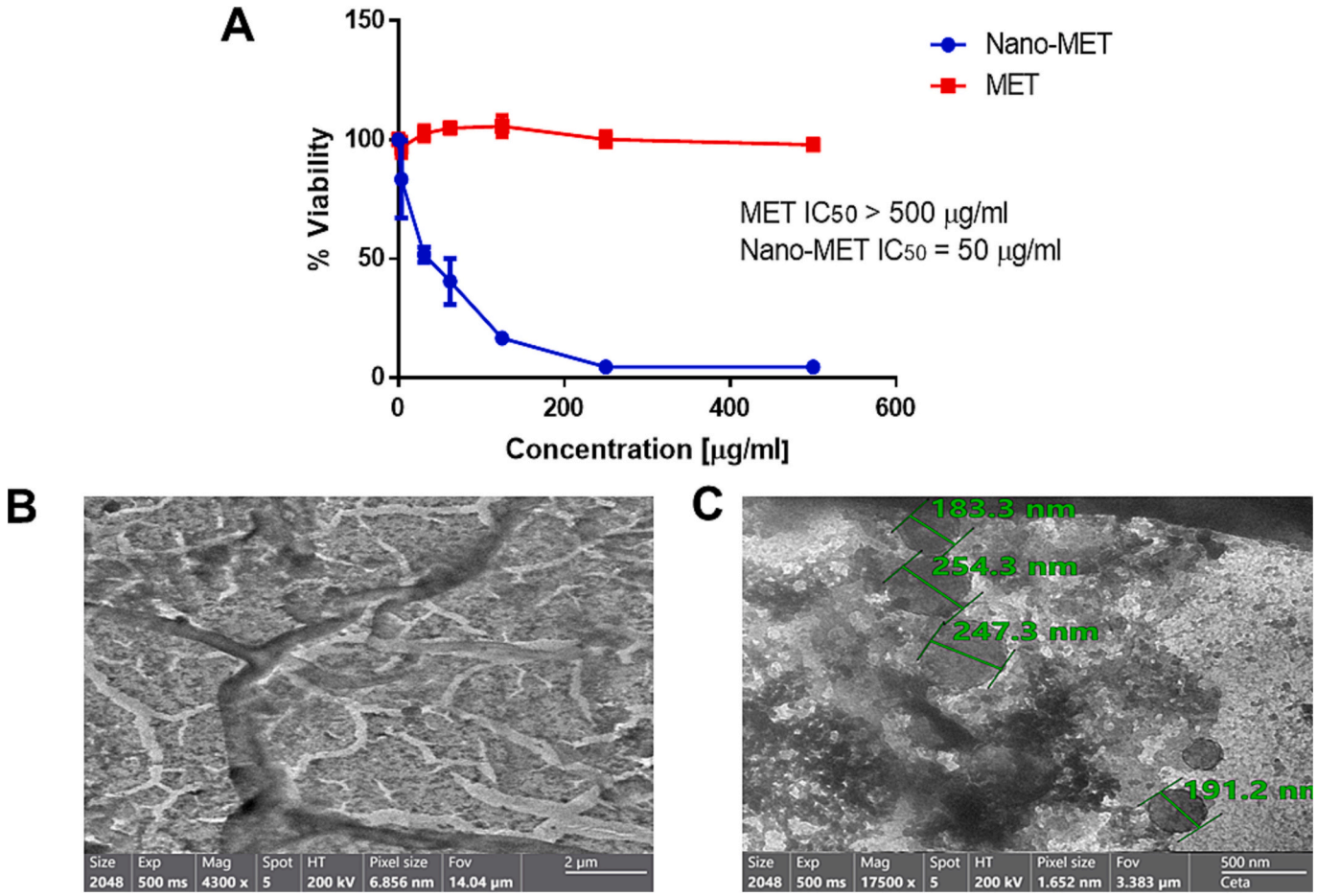

Fig. 3. (A) MTT assay showing the effect of MET and Nano-MET on HEP-2 cell viability. HEP-2 cells were exposed to serial dilutions of both treatments (500–3.9 µg/mL) for 72 h. Data are presented as a percentage of the untreated control. The error bars represent the standard deviation (SD) ($n = 6$). (B) TEM micrographs of HEP-2 cells following 72 h incubation with Nano-MET showing cells embedded in resin and imaged on a grid. (C) Nano-MET vesicles of around 200 nm seen entrapped inside the cancer cells.

Nano-MET formulation.

To ensure the safety of the Nano-MET formulation on blood cells, erythrocyte hemolysis test (Mazzarino et al., 2015) was performed. The results showed that the Nano-MET formulation was hemocompatible at concentrations of 25 μg/mL, 50 μg/mL and 100 μg/mL (Supplementary data A.1).

In addition, uptake of Nano-MET was confirmed using TEM imaging. As shown in Fig. 3B and C, nanovesicles of a diameter around 200 nm were seen entrapped inside HEP-2 cells.

3.3. Apoptosis assay and cell cycle analysis

To assess the role of apoptosis in the cytotoxic effects exerted by MET or Nano-MET on HEP-2 cells, Annexin *V*/PI staining was employed as previously described. Results (Fig. 4) showed that the treatment with Nano-MET induced significant cell death when compared to treatment with MET as well as the control ($p < 0.001$). Cells co-cultured with MET at a concentration of 50 μg/mL showed significant increase in the percentage of cells in the early apoptosis phase and significant decrease in the live cells. The percentage of viable cells, early apoptotic, late apoptotic, and necrotic cells in the MET group were 95.49 ± 0.27, 3.22 ± 0.21, 0.39 ± 0.05, 0.90 ± 0.16, respectively. In comparison, treatment of cells with Nano-MET at the same concentration significantly increased percentage of cells in early and late apoptosis phases causing more significant decrease in the percentage of live cells. The percentages of viable cells, early apoptotic, late apoptotic, and necrotic cells in the Nano-MET group were 93.70 ± 0.27, 5.5 ± 0.17, 0.76 ± 0.07, 0.33 ± 0.07, respectively.

Next, we investigated the progression of the cell cycle following treatment with MET and Nano-MET. Results (Fig. 5) revealed that cells co-cultured with Nano-MET had a significantly higher cell count in the G0/G1 phase and a significantly lower cell count in the S phase than cells co-cultured with MET, which exhibited no significant changes compared to the control group. A 72-h treatment of HEP-2 cells with Nano-MET increased the total number of cells in the G0/G1 phase by 8.38% ($P < 0.001$ vs. control), accompanied by approximately same percentage of reduction in S phase ($p < 0.001$ vs. control).

3.4. RT-qPCR results of apoptosis markers, Cyclin D1 and mTOR

Results (Fig. 6) revealed that cells treated with MET showed higher expression of apoptosis-related markers including BAX, caspase-3, caspase-8, and caspase-9 compared to the control group with mean fold change values of 1.52 ± 0.13 vs. 1.05 ± 0.08, 9.94 ± 1.03 vs. 1.13 ± 0.08, 1.63 ± 0.14 vs. 1.05 ± 0.06 and 1.47 ± 0.09 vs. 1.05 ± 0.06, respectively. Cells treated with MET showed a decrease in the anti-apoptotic marker BCL-2 expression ($p < 0.001$) compared to the control group with mean values of 0.93 ± 0.26 vs. 1.07 ± 0.08, respectively. Cells treated with Nano-MET showed the most significant increase of the apoptosis-related markers (BAX, caspase-3, −8, and −9) with mean values of 1.94 ± 0.22 ($p < 0.05$), 13.75 ± 1.39 ($p < 0.01$), 4.15 ± 0.56 ($p < 0.001$) and 2.23 ± 0.20 ($p < 0.01$), respectively. In addition, a decrease in the anti-apoptotic marker BCL-2 expression with a mean value of 0.03 ± 0.01 ($p < 0.001$) was observed when compared to the control and MET groups. Furthermore, MET and Nano-MET caused a significant decrease in the expression of cyclin D1 ($p < 0.01$)

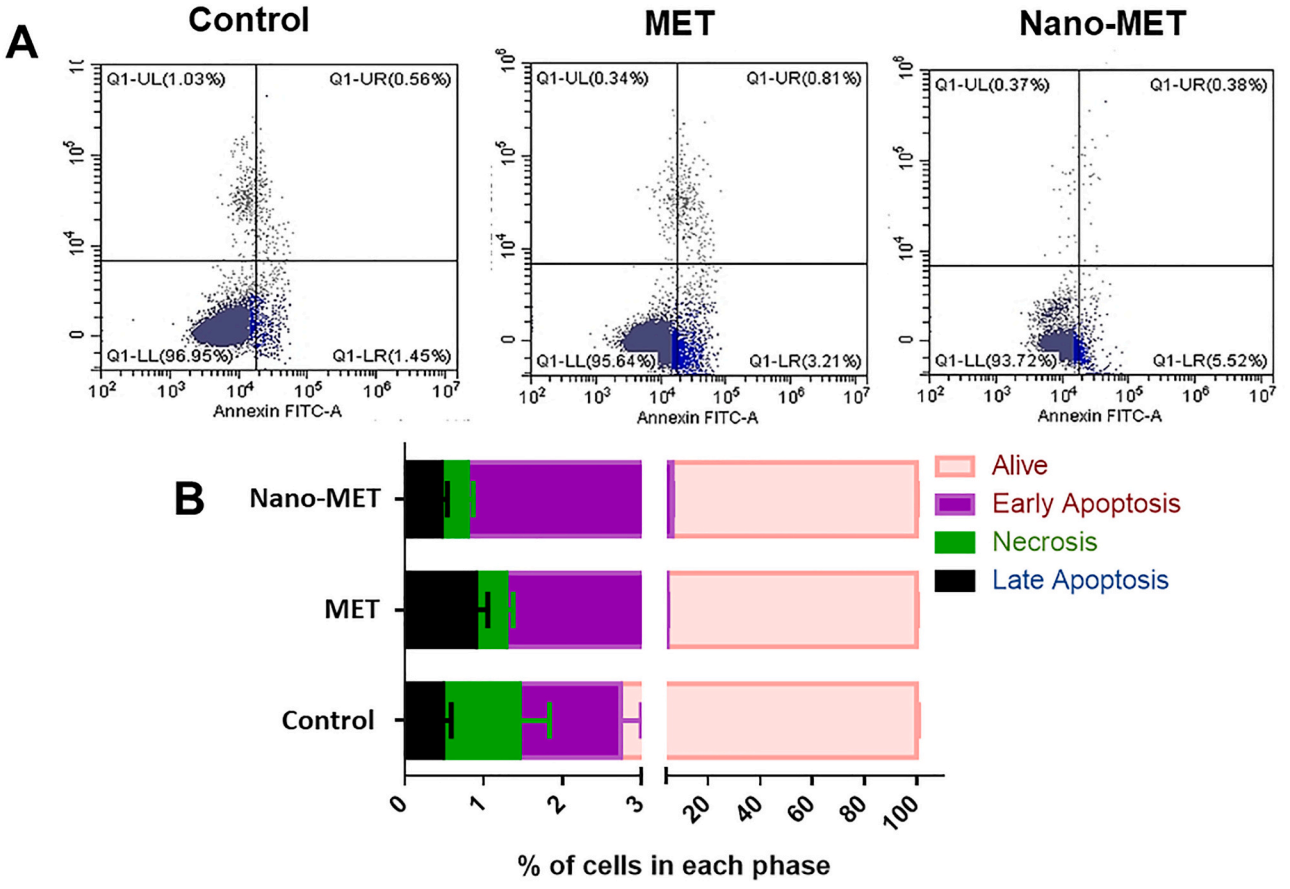

Fig. 4. Annexin V/PI apoptosis assay showing the effect of Nano-MET and MET on the percentage of apoptosis in HEP-2 cells. (A) Dot plots (Annexin V-FITC versus PI) showing the population of viable cells (LL), early apoptotic cells (LR), late apoptotic cells (UR), and necrotic cells (UL) after treatment with Nano-MET or MET for 72 h. (B) Bar chart showing the percentage of cells in each phase. Nano-MET triggered a higher percentage of cells in early and late apoptosis in HEP-2 cells than MET. Results are presented as mean ± SD. One-way ANOVA and Tukey's *post-hoc* statistical analyses were employed.

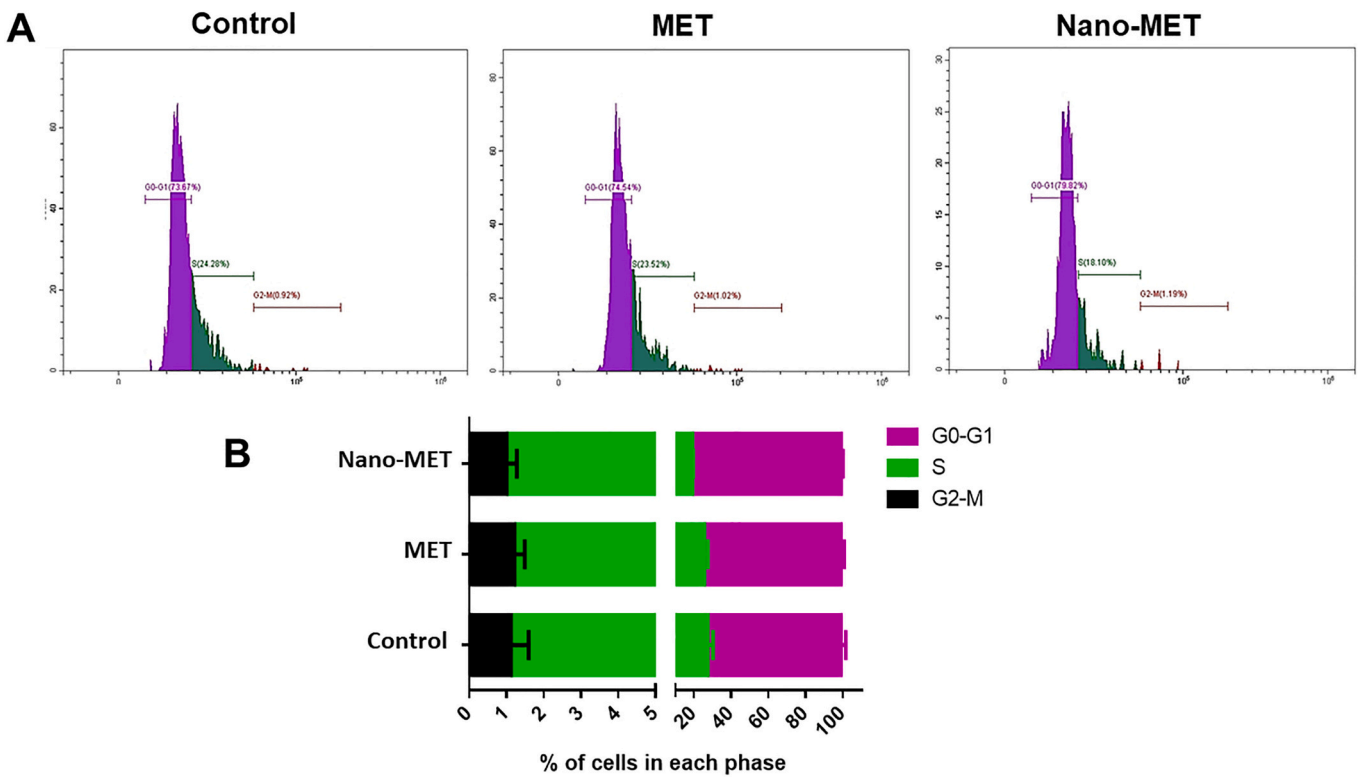

Fig. 5. Analysis of cell cycle progression of HEP-2 cells following treatment with MET and Nano-MET for 72 h. (A) Histograms showing the distribution of the cell population in the different cell cycle phases. (B) Bar chart showing the percentage of cells in each cell cycle phase. Nano-MET showed the highest percentage of cells arrested in the G0/G1 phase. Results are shown as mean ± SD. Statistical analysis was done using One-way ANOVA followed by Tukey's *post-hoc* test.

compared to the control group with mean values of 0.31 ± 0.07 and 0.011 ± 0.003 vs. 0.97 ± 0.11, respectively. Finally, MET caused a decrease in mTOR mRNA levels compared to the control group with mean values of 0.23 ± 0.04 vs. 0.97 ± 0.10, respectively. While Nano-MET significantly ($p < 0.05$) decreased mTOR levels to 0.02 ± 0.01.

3.5. The expression of apoptosis related genes BAX and BCL-2 using Western blotting

Results (Fig. 7) showed that the expression of BAX was significantly ($p < 0.001$) increased in cells co-cultured with Nano-MET when compared with the MET and control groups. In contrast, the anti-apoptotic gene BCL-2 decreased significantly in the Nano-MET group, when compared to MET and control groups. Our data revealed that BCL-2 was downregulated by approximately 1.57 folds and BAX was upregulated by approximately 1.88 folds after treatment with Nano-MET, compared to the control. Cells co-cultured with MET showed decreased expression of BCL-2 and increased expression of BAX as well, however, these changes were not statistically significant.

3.6. Immunofluorescence staining of the proliferation marker Ki67

Results (Fig. 8) showed that the untreated HEP-2 cells possessed a homogeneous intense expression of Ki67 with high fluorescence intensity (+++) and membranous localization. A reduction in both the percentage of Ki67 positive cells as well as the intensity of staining (yellow arrows) was observed in cells co-cultured with MET and Nano-MET. However, Nano-MET treated cells showed marked reduction of Ki67 protein expression. Staining quantification results showed that HEP-2 cells co-cultured with Nano-MET possessed the lowest proportion of positively stained Ki67 cells ($p < 0.01$) compared to cells co-cultured with MET and the control. The proportion of Ki67-positive cells with MET and Nano-MET treatment is significantly ($p < 0.001$) lower than the control by 2.46 and 3.15 folds, respectively (Fig. 8B).

3.7. Molecular Target Prediction and Pathway Enrichment Analysis

MET protein targets were initially predicted and classified with the aid of Swiss Target Prediction (Table 4). After that, with the help of the DisGeNET hub, four hundred and fifty-two genes were recognized as laryngeal carcinoma-associated genes (C0595989). The Venn diagram plot showed that the shared genes between MET gene targets and laryngeal carcinoma-associated genes included EGFR, ESR2, NOS3, and S100B (Fig. S2).

Toward better dissection at the genome-wide level of MET target-function interactions, Boolean network modeling and pathway enrichment analysis were performed. Based on the Voronoi tessellation analysis, a FoamTree reactome map was constructed to illustrate the top pathways affected in response to MET (Fig. S3).

The pathway enrichment analysis results revealed that the 49 gene targets stimulated by MET were identified in 879 reactome pathways, hit by at least one of them. Among the top 25 significantly major enriched pathways are; (A) metabolism (specifically, nucleotide, purine, and pyrimidine metabolism, Nudix-type (NUDT) hydrolase enzymes and carbon dioxide hydration), (B) hemostasis (specifically, dissolution of fibrin clot), and (C) innate immune system (specifically, neutrophil degranulation) with a false discovery rate (FDR) of <0.00001% (Fig. 9, Table 4).

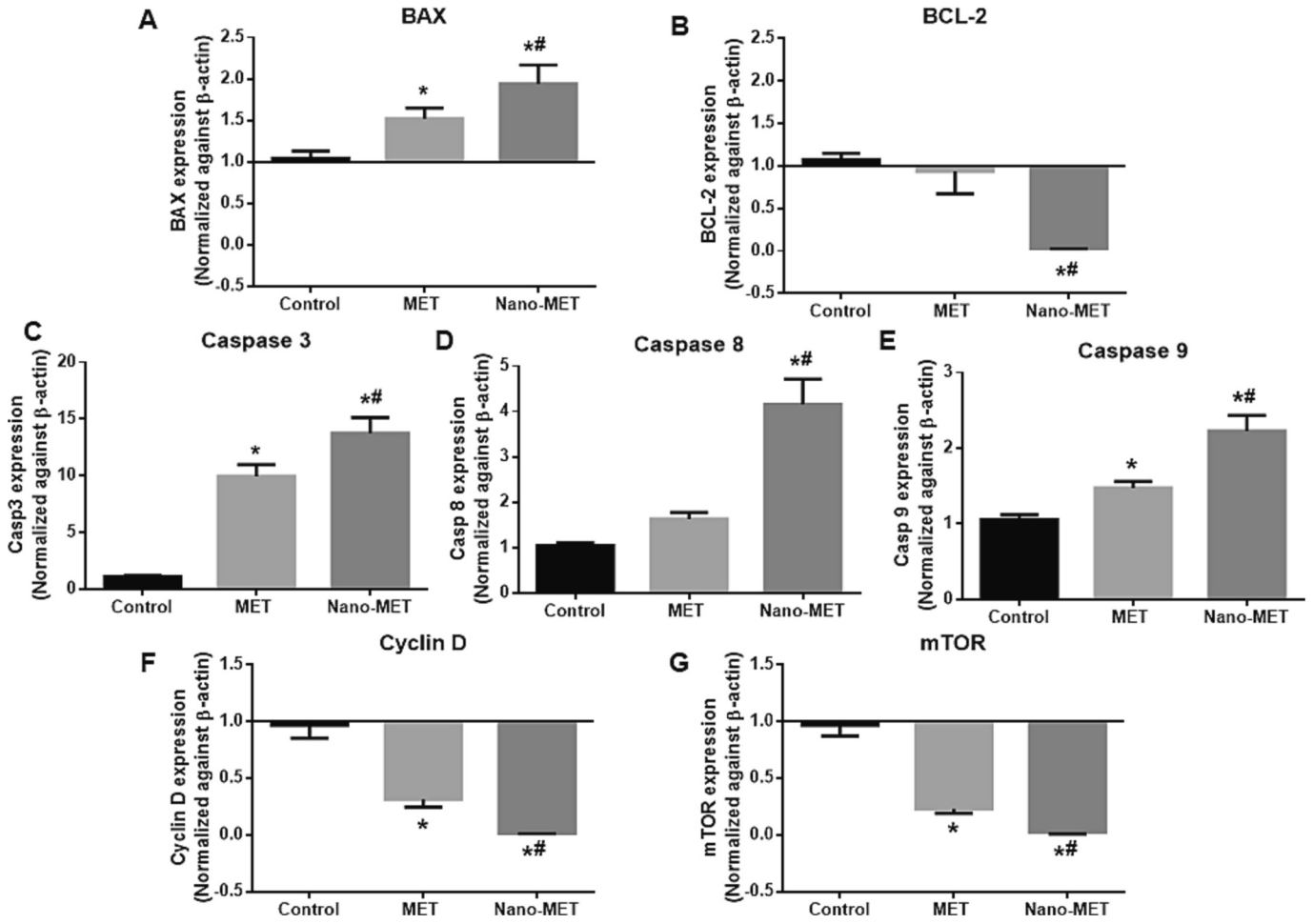

Fig. 6. Bar charts showing the fold change in mRNA levels of key apoptotic proteins, mTOR and cyclin D1 (measured with RT-qPCR and calculated using $2^{-\Delta\Delta CT}$ method) of HEP-2 cells following treatment with MET and Nano-MET. (A) Bax, (B) BCL-2, (C) Caspase-3, (D) Caspase-8, (E) Caspase-9, (F) Cyclin D1 and (G) mTOR. Results are shown as mean ± SD. Statistical analysis was done using One-way ANOVA followed by Tukey's *post-hoc* test. *$p < 0.05$ compared to the control group; #$p < 0.05$ compared to the MET group. All samples were done in triplicates ($n = 3$) and the experiment was repeated three times.

4. Discussion

Head and neck squamous cell carcinoma (HNSCC) is considered a major public health concern, thus, an urgent need for novel treatment approaches is required in order to achieve organ preservation, higher survival rates and more efficient therapies (Busch et al., 2015). Since MET is widely used in the treatment of type II diabetes mellitus (Rena et al., 2017) in addition to its safety, tolerability, and availability, it became an excellent candidate for drug repurposing. The most intriguing is its potential use as an anticancer agent. A pharmaco-epidemiological study conducted in 2005 revealed a significantly reduced cancer risk in diabetic patients receiving MET (Evans et al., 2005). In addition, several clinical trials confirmed the promising anti-neoplastic potential of MET (Chae et al., 2016; De Flora et al., 2016), however, its exact mechanism of action is still to be fully unraveled (Huynh et al., 2022). It was reported that one of the main targets of MET in cancer cells is the activation of the cellular energy sensor, AMPK (Guo et al., 2016; Han et al., 2013; Salani et al., 2012; Wang et al., 2015). MET influences mitochondrial respiration and alters the ratio of ATP/AMP due to a decrease in ATP levels, resulting in the activation of AMPK (Tawfik et al., 2022). Upon activation, AMPK inhibits mTOR, a key regulator for the energy consuming cellular processes and cellular growth. The combination of increased phosphorylation of AMPK and inhibition of mTOR inhibits cellular proliferation and growth (Jang et al., 2014). AMPK is also capable of directly inhibiting raptor, the mTOR-associated regulatory protein, that regulates cell growth, proliferation, and metabolism (Meng, 2014).

The use of nanocarriers as platforms to formulate MET could achieve various benefits including: prolonged duration of action, increased cellular uptake, and accumulation in tumor tissues as well as increased potency against different types of cancer (Chen et al., 2020). As a result, MET-encapsulated nano-drug delivery systems were repeatedly reported to possess enhanced therapeutic efficacy against many types of neoplasms including liver, colon, lung, and breast cancers (Arafa et al., 2018; Kumar et al., 2015; Osama et al., 2020; Shukla et al., 2019). The work presented herein utilized spanlastics, a new nanoformulation drug delivery system, to encapsulate MET.

MET-loaded nanospanlastics were fabricated by ethanol injection method using Span® 60 which is a nonionic lipophilic surfactant (HLB =4.7). Span® 60 possesses saturated and lipophilic alkyl chains that promote the formation of mono and/or multi-lamellar vesicles. The fabricated nanovesicles also contain an edge activator (Tween® 80) with or without a surfactant permeation enhancer (Transcutol® P), that we named S2 and S1, respectively. Both promote vesicle elasticity, resulting in systems with disrupted packing that can squeeze through skin pores or the cell membranes (Fahmy et al., 2018). Similar to our study, Fahmy *et al.* loaded haloperidol into spanlastics using the ethanol injection method, they used Span® 60 and Tween® 80 as edge activators. Their haloperidol-loaded penetration enhancer-containing spanlastics (PECSs) showed increased transdermal permeation with sustained release of the drug.

Next, we fully characterized the synthesized MET spanlastics and

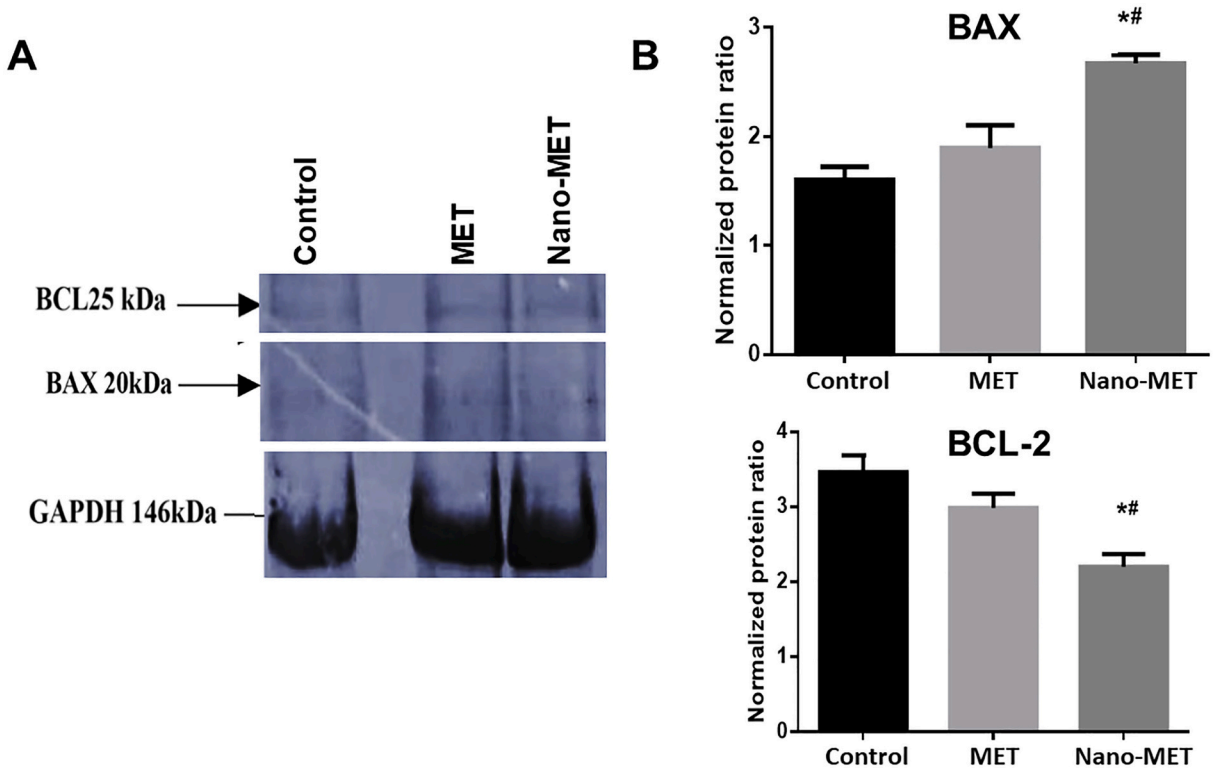

Fig. 7. The expression of apoptosis related genes measured with Western blotting in HEP-2 cells following treatment with MET and Nano-MET for 72 h. (A) Images of the Western blots showing the expression of BAX at 20 KDa, BCL-2 at 25 KDa and the housekeeping control GAPDH at 146 KDa. (B) Bar chart showing densitometry analysis of the apoptosis related genes: BAX and BCL-2 normalized to GAPDH. Results are shown as mean ± SD. Statistical analysis performed using One-Way ANOVA followed by Tukey's *post-hoc* test.

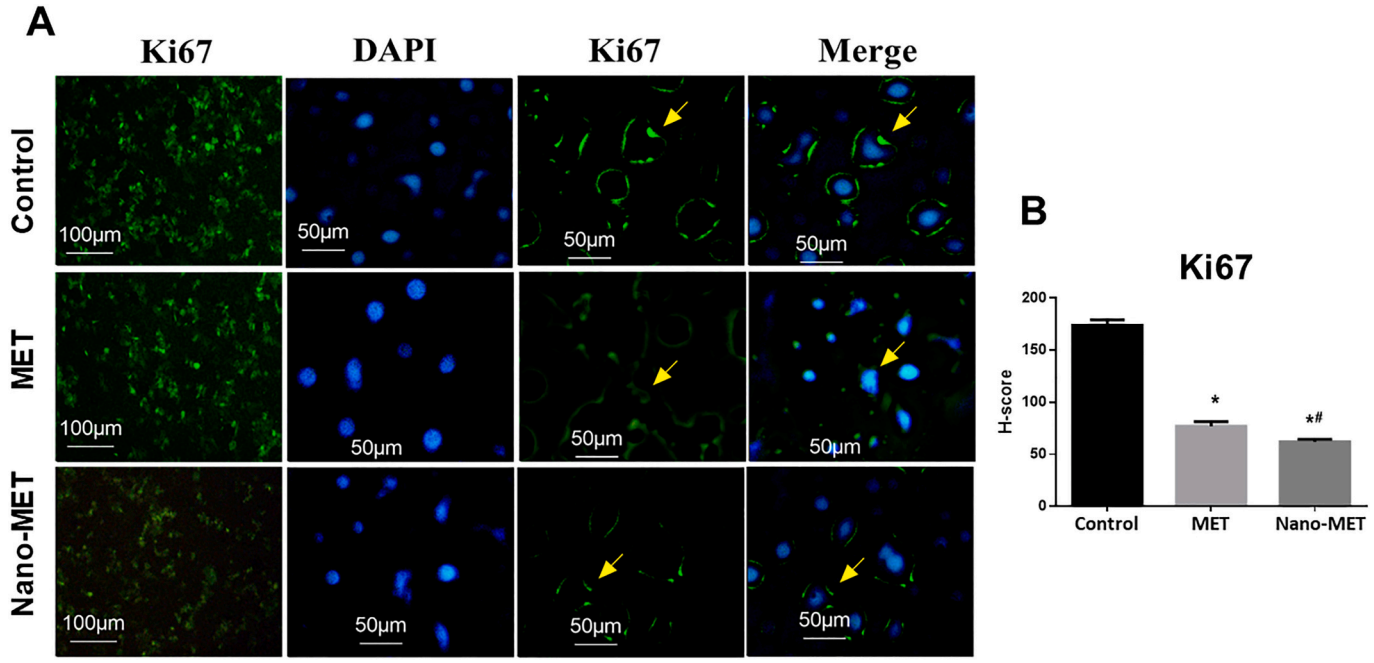

Fig. 8. Expression of Ki67 protein in HEP-2 cells detected by immunofluorescence staining following incubation with MET and Nano-MET for 72 h. (A) Florescent photomicrographs showing a reduction in both the percentage of Ki67-positively stained cells as well as staining intensity (yellow arrows) of Ki67 in cells co-cultured with both treatments, higher reduction was observed with Nano-MET group. Nuclei were counterstained with DAPI and the original magnification was 100× and 400×. (B) Bar chart showing the calculated H-score in the different treatment groups. Results are shown as mean ± SD. H-score was calculated by multiplying the sum of intensity (0–3) by the percentage of positively stained cells (0–100%). Statistical analysis was performed using One-way ANOVA followed by Tukey's *post-hoc* test. *$p < 0.05$ compared to the control group; #$p < 0.05$ compared to the MET group. All samples were done in triplicates ($n = 3$) and the experiment was repeated three times. (For interpretation of the references to colour in this figure legend, the reader is referred to the web version of this article.)

Table 4
Top 25 pathways for MET targets resulting from the pathway enrichment analysis.

Pathway name	Entities				Reactions	
	Found	Ratio	p-value	FDR*	Found	Ratio
Nucleotide catabolism	10 / 46	0.002	3.33e-16	3.06e-13	18 / 63	0.004
Metabolism of nucleotides	12 / 161	0.009	7.64e-14	3.51e-11	26 / 142	0.01
Purine catabolism	7 / 28	0.001	4.01e-12	1.23e-09	14 / 33	0.002
Phosphate bond hydrolysis by NUDT proteins	4 / 11	5.85e-04	4.50e-08	1.04e-05	7 / 17	0.001
Reversible hydration of carbon dioxide	4 / 12	6.38e-04	6.36e-08	1.17e-05	4 / 8	5.65e-04
Histamine receptors	3 / 4	0.005	2.79e-07	4.06e-05	5 / 7	4.95e-04
Amine ligand-binding receptors	6 / 88	2.13e-04	3.10e-07	4.06e-05	10 / 36	0.003
Nitric oxide stimulates guanylate cyclase	4 / 23	0.001	8.38e-07	9.64e-05	2 / 7	4.95e-04
Pyrimidine catabolism	3 / 12	6.38e-04	7.40e-06	7.55e-04	4 / 17	0.001
Defective HEXA causes GM2G1	2 / 2	1.06e-04	1.80e-05	0.002	3 / 3	2.12e-04
Dissolution of Fibrin Clot	4 / 51	0.003	1.90e-05	0.002	18 / 21	0.001
Nucleotide salvage	3 / 25	0.001	6.51e-05	0.005	4 / 22	0.002
Hyaluronan uptake and degradation	3 / 29	0.002	1.01e-04	0.007	3 / 10	7.07e-04
Hyaluronan metabolism	3 / 34	0.002	1.61e-04	0.01	3 / 13	9.19e-04
Metabolism	26 / 4364	0.232	1.63e-04	0.01	74 / 2268	0.16
ROS and RNS production in phagocytes	3 / 36	0.002	1.90e-04	0.01	1 / 45	0.003
Highly sodium permeable postsynaptic acetylcholine nicotinic receptors	2 / 7	3.72e-04	2.18e-04	0.01	2 / 2	1.41e-04
Defective factor VIII causes hemophilia A	2 / 7	3.72e-04	2.18e-04	0.01	2 / 8	5.65e-04
Highly calcium permeable nicotinic acetylcholine receptors	2 / 9	4.78e-04	3.59e-04	0.017	2 / 2	1.41e-04
Tetrahydrobiopterin (BH4) synthesis, recycling, salvage and regulation	2 / 10	5.32e-04	4.42e-04	0.019	3 / 16	0.001
Highly calcium permeable postsynaptic nicotinic acetylcholine receptors	2 / 11	5.85e-04	5.34e-04	0.022	2 / 2	1.41e-04
Neutrophil degranulation	2 / 13	6.91e-04	6.08e-04	0.024	6 / 10	7.07e-04
Presynaptic nicotinic acetylcholine receptors	2 / 12	6.38e-04	6.34e-04	0.024	4 / 4	2.83e-04
Keratan sulfate degradation	2 / 13	6.91e-04	7.43e-04	0.024	2 / 7	4.95e-04

results revealed the successful synthesis of spanlastics in the nanosized range with acceptable size distribution and low PDI values. Particle size is an important factor in drug delivery systems, influencing drug loading, release rates and absorption (Badawi et al., 2020). The nanometric range of a drug delivery system could ensure the successful delivery of a nanocarrier to the tumor site (Barani et al., 2019). In addition, the PDI is a measurement of the formulation's width of size distribution and always ranges between 0 and 1. The higher the PDI, the less vesicle size uniformity in the formulation (Elsherif et al., 2017). PDI $\leq$ 0.3 corresponds to an intense and narrow peak in size distribution profile of particles (Barani et al., 2019) which was observed in both S1 and S2 MET spanlastics with S2 showing a smaller PDI value. The surfactants of choice for our spanlastics were Tween® 80 with or without Transcutol® P. Tween® 80 was deemed the most appropriate edge activator as it can produce smaller nanovesicles owing to its reduced bulkiness and unsaturation. These properties ensure its incorporation into the nanovesicles and leads to improved chain bending and consequently smaller nanoparticles (Elmowafy et al., 2019). The outcomes also revealed that adding the permeation enhancer surfactant (Transcutol® P) in S2 resulted in reduction in the particle size and PDI with a more negative zeta potential and higher DC and EE%. These favorable properties could be accredited to a decreased interfacial tension caused by increasing the surfactant concentration which aids particle partition and consequently the formation of smaller nanovesicles (Shamma et al., 2019). Our findings are in agreement with previously published data by Shamma *et al.* that reported the fabrication of retinoic acid (RA) loaded spanlastics containing Span 60, Tween 20 with or without Transcutol®. RA-spanlastics prepared with Transcutol showed a smaller PS, a more negative ZP and most importantly a 2-fold improvement of skin deposition in newborn mice compared to their non-Transcutol® counterparts and the clinically used commercial drug (Acretin®) (Shamma et al., 2019). In our study, both spanlastics (S1 and S2) were negatively charged due to the presence of Span 60 which possess partial negative polar heads directed toward the aqueous dispersion medium (Elmowafy et al., 2019). Moreover, the addition of the surfactant permeation enhancer (Transcutol® P) in the formulation S2 resulted in a more negative ZP due to its smaller hydrodynamic diameter and thus a slower migration velocity (Mekkawy et al., 2022).

Furthermore, DC and EE% analyses revealed that both nanoformulations were able to encapsulate a reasonable amount of MET. This could be attributed to the length of the chain as well as the size of the hydrophilic head group of the nonionic surfactant. As previously reported, the presence of Span 60, a long-chain surfactant, produces high entrapment efficiency in nanovesicles (Teaima et al., 2020) in addition to the long alkyl chain and the large hydrophilic moieties of Tween® 80 (Almuqbil et al., 2022). We also observed a more sustained release of MET from spanlastics compared with the free drug, this could be explained by the elevated transition temperature and the long-chain of Span 60 that leads to the formation of a more rigid and a less permeable bilayer (Abdelbari et al., 2021). In addition, the attractive forces within the phospholipid bilayer cause a more delayed drug release from spanlastics (Alaaeldin et al., 2021). Our findings agree with previously published data that reported the sustained release profiles of spanlastics compared to the free drugs (Abdelrahman et al., 2017; Fahmy et al., 2018; Mekkawy et al., 2022). Abdelrahman *et al.* formulated the anti-psychotic drug, risperidone, into nanospanlastics composed of Span and polyvinyl alcohol. The risperidone-spanlastics achieved a delayed drug release, better nasal permeation and enhanced brain distribution (Abdelrahman et al., 2017). Furthermore, Mekkawy *et al.* proposed a new combination therapy for breast cancer using the non-steroidal aromatase inhibitor (letrozole) and polyphenolic flavonoid (quercetin) by loading them into spanlastics using edge activators (such as Brij 35, Tween 80 and Cremophor RH40). The drug loaded spanlastics showed sustained drug release, enhanced permeation through rat skin and increased cytotoxicity on MCF-7 breast cancer cells (Mekkawy et al., 2022).

Subsequently, we conducted a number of proof-of-concept biological studies using the S2 Nano-MET formulation due to its smaller PS and PDI as well as higher EE% and ZP. First, we used the standard MTT cell viability assay to evaluate the cytotoxicity of Nano-MET compared to MET on HEP-2 laryngeal cancer cells. MET exhibited an IC_{50} value higher than the highest tested concentration of 500 μg/mL. Interestingly, Nano-MET produced a significantly more potent IC_{50} value of 50 μg/mL, demonstrating an enhanced anti-proliferative potency of the nanospanlastics formulation compared to the free drug. The stronger cytotoxic effect of MET spanlastics could be due to the protective role and the unique properties of the nanospanlastics that offer higher cell membrane permeability and elasticity provided by the edge activators

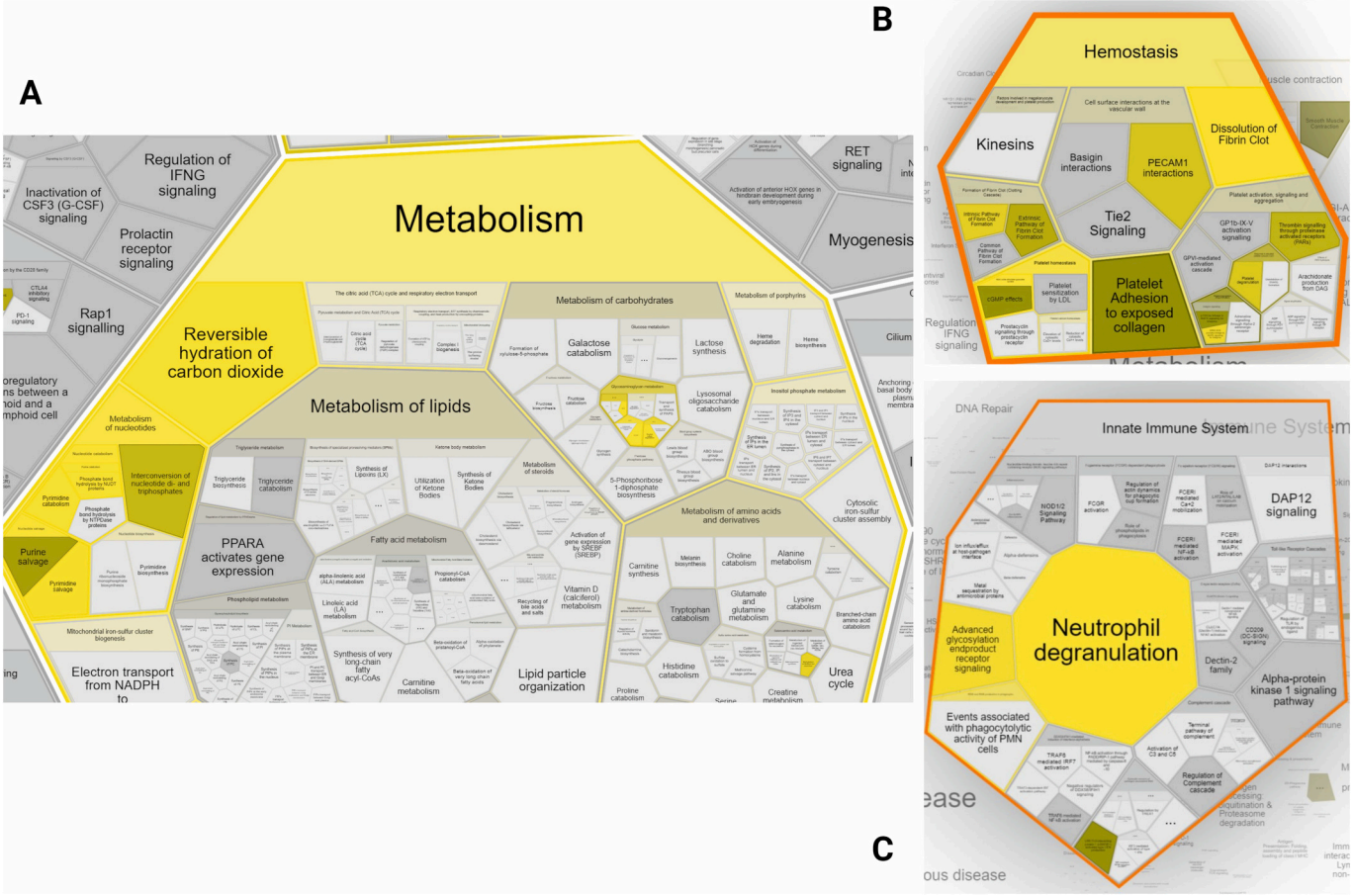

Fig. 9. The Voronoi treemaps of the top enriched pathways (A) metabolism, (B) hemostasis and (C) innate immune system influenced by the top 49 gene targets in response to MET as a repurposed anti-cancer drug.

(Alaaeldin et al., 2021; Kanaani et al., 2017). Edge activators increase the bilayer fluidity and deformability of the vesicle facilitating their diffusion through the cell membrane and augmenting the cellular accumulation of the drug (Alaaeldin et al., 2021). Previous studies also reported the enhanced cellular uptake and improved cancer cytotoxicity of Span 60 containing nanoformulations (Fatemizadeh et al., 2022; Shaker et al., 2015) such as the work of Mehanna *et al.* They prepared thymoquinone-loaded nanoparticles with enhanced anticancer effect and improved ability of internalization into cancer cells (Mehanna et al., 2020). We also showed that the formulated Nano-MET was hemocompatible and was indeed taken up by HEP-2 cells as observed with TEM.

Afterwards, we examined the effect of MET and Nano-MET on the cell cycle. The uncontrolled progression of the cell cycle is one of the hallmarks of cancer. Consequently, its inhibition represents a main therapeutic target (He et al., 2021). The results of our study showed that Nano-MET treatment led to a cell cycle arrest in the G0/G1 phase as well as a significant decrease in the S phase compared to the untreated control. This was in accordance with previous studies which demonstrated that MET caused the accumulation of cells in the G0/G1 (Kobayashi et al., 2013; Queiroz et al., 2014; Zhao et al., 2022) which is thought to be regulated through oxidative stress along with AMPK activation and cyclin D suppression (Yenmiş et al., 2021; Zhao et al., 2022). Cyclin D1 combines with CDK2 and CDK6 to form a complex, driving cancer cells from the G1 phase to the S phase and thus promoting cell proliferation (Zhao et al., 2022). Our results showed a significant decrease in cyclin D1 mRNA levels in cells treated with MET and Nano-MET as measured with RT-qPCR. Nano-MET caused a significant 100-fold decrease in cyclin D1 levels compared to the control while MET alone showed a 3.33-fold decrease. Our findings are consistent with previously published data that reported the downregulation of cyclin D1 expression by MET (Zhao et al., 2022).

Consequently, we assessed the effect of MET and Nano-MET in the apoptosis Annexin *V*/PI assay as well as on the expression of the key apoptosis regulatory proteins (BAX, BCL-2, caspase-3, −8, and − 9). BCL-2 protein family (such as, BAX and BCL-2 proteins) plays a critical role in maintaining the mitochondrial membrane integrity and thus the regulation of apoptosis. BAX induce apoptosis *via* the disruption of the mitochondrial membrane while the anti-apoptotic BCL-2 has an opposite effect (Zhao et al., 2022). The caspase family of proteins plays a vital role in the induction of apoptosis *via* both the intrinsic and extrinsic pathways (Van Opdenbosch and Lamkanfi, 2019). In the present study, treatment of HEP-2 cells with Nano-MET induced significant cell death when compared to treatment with MET or the control. Furthermore, the expression of the proapoptotic BAX was upregulated, unlike the anti-apoptotic BCL-2, which was downregulated following treatment with Nano-MET as confirmed with both RT-qPCR and Western blotting analysis. MET and Nano-MET caused a 9.94 and 13.75-fold increase in the levels of the apoptotic executioner, caspase-3 as measured with RT-qPCR. While caspase-8, a key player in the extrinsic apoptosis pathway (Van Opdenbosch and Lamkanfi, 2019), was increased by 1.63 and 4.15 folds with MET and Nano-MET, respectively. Interestingly, the intrinsic pathway regulator (caspase-9) was also elevated by 1.47 and 2.22 folds with MET and Nano-MET, respectively. Our results are in agreement with the findings of Shukla *et al.* that developed MET liposomal vesicles that exhibited enhanced cytotoxicity at reduced doses against breast cancer (Shukla et al., 2019). These effects were caused by increased expression of caspase-3 leading to profound apoptosis in cells treated with liposomal MET compared to the free drug and the control (Shukla

et al., 2019). The study also reported that cells treated with liposomal MET possessed high levels of p-AMPK and reduced levels of p-mTOR as compared to MET (Shukla et al., 2019). In addition (Wang et al., 2021b) also reported the downregulation of mTOR and p-mTOR in oral squamous cell carcinoma (OSCC) cells treated with MET. Similarly, we also showed that the expression of mTOR was significantly reduced by MET and nano-MET by 4.34 and 43.47 folds, respectively, as measured using RT-qPCR.

Finally, we evaluated one of the key proliferative markers, Ki67 (Morse et al., 2019) using immunofluorescent staining done on HEP-2 cells. Our results revealed a significant reduction in the expression of Ki67 in cells treated with MET and Nano-MET compared to the control with a stronger downregulation observed with Nano-MET. Our results were similar to Zhao *et al.* that reported a significant downregulation of Ki67 in OSCC tumor xenografts following treatment with MET (Zhao et al., 2022).

The combined pathway enrichment analysis-Reactome mining facilitates the capture of the connections in a computable data model between genes, proteins, and small molecules affected by MET treatment. Therefore, in an attempt to investigate the different possible pathways implicated in MET's anticancer effect on the cells, pathway enrichment analysis was performed. The PEA-Reactome mining coupled approach revealed high enrichment of several pathways as a result of treatment with MET including metabolism: specifically, nucleotide, purine and pyrimidine metabolism, as well as the implicated Nudix-type (NUDT) hydrolase enzymes and carbon dioxide hydration, in addition to other pathways such as hemostasis and the innate immune system.

Deranged nucleotide metabolism is a pan-cancer metabolic dependence that significantly impacts almost all malignant cell activities across many cancer types. Nucleotides fuel a wide range of processes that are active more frequently in cancer cells in addition to their canonical function as substrates for nucleic acid synthesis. As a result, nucleotide synthesis inhibitors have a lot of untapped potential as components of combination therapy plans (Mullen and Singh, 2023). In general, metabolic reprogramming is intensified during cancer to support cell survival and proliferation in the face of alterations to the internal and external milieu. For example, it is common knowledge that cancer cells seek to alter their metabolism to increase the flux of purine and pyrimidine syntheses to maintain aggressive growth (Schiliro and Firestein, 2021). Metformin was previously reported to alter nucleotide metabolism thus affecting susceptibility of OSCC cancer cells to different anticancer nucleoside analogs (Mynhardt et al., 2018). MET induced resistance to 5-fluorouracil (5-FU) *via* the increased expression of thymidine kinase 1 and thymidylate synthase (key players in 5-fluorouracil (5-FU) resistance). On the contrary, MET enhanced the cytotoxicity of gemcitabine by elevating the expression of deoxycytidine kinase (DCK) (Mynhardt et al., 2018). DCK is a key player in the nucleoside salvage pathway and also catalyzes the phosphorylation and activation of gemcitabine (Aksoy et al., 2008).

Since purine nucleotides are essential and required for tumor cell growth, tumor cells have increased levels of purines and enzymes for the de novo purine synthesis pathway. Meanwhile, purines function as strong regulators of the immune cells' responses and cytokine release *via* various receptor subtypes, which is crucial for oncogenesis and tumorigenesis. Targeting purine degradation has been utilized to treat cancer because increased purine degradation reduces the amount of purines available for nucleotide synthesis, which prevents cancer cells from proliferating (Yin et al., 2018). Pyrimidine metabolic remodeling also promotes the growth of tumors and creates metabolic vulnerabilities that can be addressed in the treatment of cancer (Wang et al., 2021a). Shatova *et al.* reported that MET significantly alters purine catabolism in breast cancer (Shatova et al., 2016). MET treated breast cancer patients, despite the increased activity of adenosine deaminase enzyme in tumor tissues, its substrate (adenosine) levels were not sufficiently reduced unlike the products (hypoxanthine and inosine) which were significantly increased (Shatova et al., 2016).

On another side, Nudix-type (NUDT) hydrolase enzymes are also key players in cancer progression and were identified as an independent prognostic factor in several types of cancer (Wang et al., 2020; Wang et al., 2017). It was previously shown that their expression levels are associated with cancer aggressiveness (Wright and Beato, 2021). Moreover, their knockdown in cancer cells decreased cell proliferation (Iyama et al., 2010). To the best of our knowledge this pathway has not been linked to MET before which highlights the importance of unraveling these unstudied pathways using the PEA-reactome analysis presented herein.

One of the main pathways found to be affected by MET in the PEA-Reactome mining coupled approach is the carbon dioxide hydration. Previous reports indicate the relationship between pH regulation and tumor cell survival and proliferation. These reports show the direct implication of carbonic anhydrases in these processes (Mboge et al., 2018). Carbonic anhydrase is induced by hypoxia and is implicated in tumor invasiveness and drug resistance (Pastorekova and Gillies, 2019). It is a poor prognostic factor in breast cancer (Rezuchova et al., 2023). Metformin was previously reported to inhibit carbonic anhydrase activity thus affecting pH and inducing cancer cell death (Ismail and Amodu, 2016).

Of the other pathways that were found to be affected by MET in our pathway enrichment analysis are those involved with the innate immune system. Neutrophils are essential for the activation and control of both innate and adaptive immunity as well as infection defense. Tumor-associated neutrophils have become a significant part of the tumor microenvironment in cancer. They can do two jobs in this situation. These neutrophils can contribute to inflammation that promotes tumor growth by stimulating angiogenesis, extracellular matrix remodeling, metastasis, and immunosuppression. Neutrophils, on the other hand, can also mediate antitumor responses by directly destroying tumor cells and taking part in cellular networks that promote antitumor resistance. The dual potential of the tumor-associated neutrophils in the tumor microenvironment is supported by neutrophil variety and plasticity (Jaillon et al., 2020). Current research shows that increased neutrophil-to-lymphocyte ratios are a marker of poor overall survival in cancer, thus pointing to neutrophils as a possible therapeutic target and biomarker for cancer disease status (Mollinedo, 2019). In patients with diabetes and polycystic ovarian disease, MET has been demonstrated to lower neutrophil counts and neutrophil-lymphocyte ratios, respectively (Cameron et al., 2016; Ibáñez et al., 2005). It was also reported to increase neutrophil chemotaxis and degranulation (Park et al., 2013).

Hemostasis pathways were also of the main pathways affected by MET. The end result of the blood coagulation cascade is fibrin. Fibrin clots do not occur naturally, but they are associated with a number of pathological diseases, including infarctions of the heart (Silvain et al., 2011) or brain (Skaf et al., 2005), traumas (Drew et al., 2001), acute inflammation (Levi et al., 2004), cancer invasion (Idell et al., 1995), and metastasis (Im et al., 2004). It is known that tumor vascular permeability and tumor-induced blood coagulation, which cause the deposition of insoluble fibrin in various cancer tissues (Colpaert et al., 2003; Dvorak, 2002; Hisada et al., 2013; Nagy et al., 2012; Shoji et al., 1998) involve both intrinsic (Matsumura et al., 1988) and extrinsic (Dvorak, 2002) coagulation systems. It is now understood that tissue factor (TF), the main catalyst for extrinsic blood coagulation, is crucial for the growth, invasion, and metastasis of tumors. Most human cancer cells have high levels of TF expression on their surfaces (van den Berg et al., 2012), and this expression is associated with a worse prognosis in a number of cancers (Nitori et al., 2005; Seto et al., 2000; Ueno et al., 2000).

Several studies demonstrated the effect of MET on fibrin clot formation. Standeven *et al.,* showed that MET affect thrombin activity, fibrin formation and polymerization (Standeven et al., 2002). Xin *et al.,* also demonstrated that it inhibits platelet activation thus preventing thrombosis (Xin et al., 2016). In a recent study, MET was proven to reduce tissue factor activity which was previously associated with poor

cancer prognosis (Witkowski et al., 2021).

5. Summary and conclusions

To the best of our knowledge, the encapsulation of MET into the unique spanlastics nanoformulations is a poorly investigated area especially in HNSCC which highlights the importance of our study. To sum up, the results presented herein showed that the encapsulation of MET in uniform nanosized spanlastics was successful and possessed unique anticancer properties compared to the free drug. This could be attributed to the unique properties of spanlastics that led to: (a) enhanced drug permeability; (b) improved cell membrane diffusion and (c) increased accumulation of the drug within the cells. Nano-MET possessed a significantly more potent cytotoxic effect on HEP-2 cells and caused cell cycle arrest at the G0/G1 phase. In addition, Nano-MET induced apoptosis through enhanced expression of proapoptotic protein markers (BAX, caspase-3, −8, and − 9), downregulation of anti-apoptotic BCL-2 and the proliferative proteins (Ki67, cyclin D, and mTOR). To characterize the role of MET as an anticancer drug, reactome analysis was also performed. The results revealed high enrichment of several pathways including nucleotides (purine and pyrimidine) metabolism, Nudix-type (NUDT) hydrolase enzymes, and carbon dioxide hydration, as well as additional pathways like hemostasis and the innate immune system. These pathways were previously reported to be involved in cancer cell growth and proliferation.

In conclusion, the promising findings of our proof-of-concept study could pave the way for future research into the encapsulation of the repurposed MET into spanlastics for the treatment of many cancers.

Supplementary data to this article can be found online at https://doi.org/10.1016/j.ijpx.2023.100215.

CRediT authorship contribution statement

SNR contributed to the experimental design, execution, data analysis and manuscript preparation. **SAEW** contributed to experimental work and manuscript preparation. **NMB** contributed to experimental design, execution, data analysis and manuscript preparation. **MMS** conducted reactome analysis, data interpretation and manuscript preparation. **MRAA** contributed to the experimental design, execution, data analysis and manuscript preparation.

Funding

The authors declare that no funds, grants, or other support were received during the experimentation or preparation of this manuscript.

Declaration of Competing Interest

The authors declare that they have no known competing financial interests or personal relationships that could have appeared to influence the work reported in this paper.

Data availability

The datasets generated during and/or analyzed during the current study are not publicly available but are available from the corresponding author upon request.

Acknowledgements

The authors would like to thank Dr. Nashwa El-Khazragy (Global Labs, Cairo, Egypt) for her technical assistance in Western blotting and immunofluorescence staining. The authors would like to extend their gratitude to Professor Mohamed Atia Omar for his insightful help in the Reactome analysis data.

References

Abdelbari, M.A., El-Mancy, S.S., Elshafeey, A.H., Abdelbary, A.A., 2021. Implementing spanlastics for improving the ocular delivery of clotrimazole: in vitro characterization, ex vivo permeability, microbiological assessment and in vivo safety study. Int. J. Nanomedicine 16, 6249.

Abdelrahman, F.E., Elsayed, I., Gad, M.K., Elshafeey, A.H., Mohamed, M.I., 2017. Response surface optimization, ex vivo and in vivo investigation of nasal spanlastics for bioavailability enhancement and brain targeting of risperidone. Int. J. Pharm. 530, 1–11.

Abdollah, M.R.A., Ali, A.A., Elgohary, H.H., Elmazar, M.M., 2023. Antiangiogenic drugs in combination with seaweed fucoidan: A mechanistic in vitro and in vivo study exploring the VEGF receptor and its downstream signaling molecules in hepatic cancer. Front. Pharmacol. 14.

Aksoy, P., Kocabas, N., Pelleymounter, L., Gilbert, J., Salavaggione, O., Eckloff, B., Wieben, E., Yee, V., Weinshilboum, R., Ames, M., 2008. Gemcitabine Pharmacogenomics: Deoxycytidine Kinase (DCK) and Cytidine Monophosphate Kinase (CMPK) Gene Sequence Variation and Functional Genomics.

Alaaeldin, E., Mostafa, M., Mansour, H.F., Soliman, G.M., 2021. Spanlastics as an efficient delivery system for the enhancement of thymoquinone anticancer efficacy: fabrication and cytotoxic studies against breast cancer cell lines. J. Drug Deliv. Sci. Technol. 65, 102725.

Alhazmi, Y.A., Aljabri, M.Y., Raafat, S.N., Gomaa, S.M., Shamel, M., 2023. Exploring the effects of low-level laser therapy on the Cytocompatibility and Osteo/Odontogenic potential of Gingival-Derived mesenchymal stem cells: preliminary report. Appl. Sci. 13, 8490.

Almuqbil, R.M., Sreeharsha, N., Nair, A.B., 2022. Formulation-by-design of efinaconazole spanlastic nanovesicles for transungual delivery using statistical risk management and multivariate analytical techniques. Pharmaceutics 14, 1419.

Ansari, M.D., Saifi, Z., Pandit, J., Khan, I., Solanki, P., Sultana, Y., Aqil, M., 2022. Spanlastics a novel nanovesicular carrier: its potential application and emerging trends in therapeutic delivery. AAPS PharmSciTech 23, 112.

Arafa, K., Shamma, R.N., El-Gazayerly, O.N., El-Sherbiny, I.M., 2018. Facile development, characterization, and optimization of new metformin-loaded nanocarrier system for efficient colon cancer adjunct therapy. Drug Dev. Ind. Pharm. 44, 1158–1170.

Badawi, N., El-Say, K., Attia, D., El-Nabarawi, M., Elmazar, M., Teaima, M., 2020. Development of pomegranate extract-loaded solid lipid nanoparticles: quality by design approach to screen the variables affecting the quality attributes and characterization. ACS Omega 5, 21712–21721.

Badawi, N.M., Attia, Y.M., El-Kersh, D.M., Hammam, O.A., Khalifa, M.K., 2022. Investigating the impact of optimized trans-Cinnamic Acid-Loaded PLGA nanoparticles on epithelial to mesenchymal transition in breast cancer. Int. J. Nanomedicine 17, 733.

Badria, F., Mazyed, E., 2020. Formulation of nanospanlastics as a promising approach for improving the topical delivery of a natural Leukotriene inhibitor (3- Acetyl-11-Keto-β-Boswellic Acid): statistical optimization. In: Vitro Characterization, and Ex Vivo Permeation Study. Drug Design, Development and Therapy, pp. 3697–3721.

Barani, M., Mirzaei, M., Torkzadeh-Mahani, M., Adeli-Sardou, M., 2019. Evaluation of carum-loaded niosomes on breast cancer cells: physicochemical properties, in vitro cytotoxicity, flow cytometric, DNA fragmentation and cell migration assay. Sci. Rep. 9, 7139.

Bezerianos, A., Dragomir, A., Balomenos, P., 2017. Computational Methods for Processing and Analysis of Biological Pathways. Springer.

Blucher, A.S., McWeeney, S.K., Stein, L., Wu, G., 2019. Visualization of drug target interactions in the contexts of pathways and networks with ReactomeFIViz. F1000Research 8.

Busch, C.-J., Tribius, S., Schafhausen, P., Knecht, R., 2015. The current role of systemic chemotherapy in the primary treatment of head and neck cancer. Cancer Treat. Rev. 41, 217–221.

Calixto, G., Bernegossi, J., Fonseca-Santos, B., Chorilli, M., 2014. Nanotechnology-based drug delivery systems for treatment of oral cancer: a review. Int. J. Nanomedicine 3719–3735.

Cameron, A.R., Morrison, V.L., Levin, D., Mohan, M., Forteath, C., Beall, C., McNeilly, A. D., Balfour, D.J., Savinko, T., Wong, A.K., 2016. Anti-inflammatory effects of metformin irrespective of diabetes status. Circ. Res. 119, 652–665.

Chae, Y.K., Arya, A., Malecek, M.-K., Shin, D.S., Carneiro, B., Chandra, S., Kaplan, J., Kalyan, A., Altman, J.K., Platanias, L., 2016. Repurposing metformin for cancer treatment: current clinical studies. Oncotarget 7, 40767.

Chen, Y., Shan, X., Luo, C., He, Z., 2020. Emerging nanoparticulate drug delivery systems of metformin. J. Pharm. Investig. 50, 219–230.

Cheng, S.-Y., Huang, Y.-C., Wen, Z.-H., Hsu, C.-H., Wang, S.-K., Dai, C.-F., Duh, C.-Y., 2009. New 19-oxygenated and 4-methylated steroids from the Formosan soft coral Nephthea chabroli. Steroids 74, 543–547.

Colpaert, C., Vermeulen, P., Van Beest, P., Soubry, A., Goovaerts, G., Dirix, L., Harris, A., Van Marck, E., 2003. Cutaneous breast cancer deposits show distinct growth patterns with different degrees of angiogenesis, hypoxia and fibrin deposition. Histopathology 42, 530–540.

De Flora, S., Ganchev, G., Iltcheva, M., La Maestra, S., Micale, R.T., Steele, V.E., Balansky, R., 2016. Pharmacological modulation of lung carcinogenesis in smokers: preclinical and clinical evidence. Trends Pharmacol. Sci. 37, 120–142.

Drew, A.F., Liu, H., Davidson, J.M., Daugherty, C.C., Degen, J.L., 2001. Wound-healing defects in mice lacking fibrinogen. Blood J. Am. Soc. Hematol. 97, 3691–3698.

Dvorak, H.F., 2002. Vascular permeability factor/vascular endothelial growth factor: a critical cytokine in tumor angiogenesis and a potential target for diagnosis and therapy. J. Clin. Oncol. 20, 4368–4380.

Eissa, M.A., Hashim, Y.Z.-Y., Mohd Nasir, M.H., Nor, Y.A., Salleh, H.M., Isa, M.L.M., Abd-Azziz, S.S., Abd Warif, N.M., Ramadan, E., Badawi, N.M., 2021. Fabrication and characterization of Agarwood extract-loaded nanocapsules and evaluation of their toxicity and anti-inflammatory activity on RAW 264.7 cells and in zebrafish embryos. Drug Deliv. 28, 2618–2633.
Elmowafy, E., El-Gogary, R.I., Ragai, M.H., Nasr, M., 2019. Novel antipsoriatic fluidized spanlastic nanovesicles: in vitro physicochemical characterization, ex vivo cutaneous retention and exploratory clinical therapeutic efficacy. Int. J. Pharm. 568, 118556.
Elsherif, N., Shamma, R., Abdelbary, G., 2017. Terbinafine hydrochloride trans-ungual delivery via nanovesicular systems. Vitro characterization and ex vivo evaluation. AAPS Pharm. Sci. Tech. 18.
Evans, J.M., Donnelly, L.A., Emslie-Smith, A.M., Alessi, D.R., Morris, A.D., 2005. Metformin and reduced risk of cancer in diabetic patients. BMJ 330, 1304–1305.
Fahmy, A.M., El-Setouhy, D.A., Ibrahim, A.B., Habib, B.A., Tayel, S.A., Bayoumi, N.A., 2018. Penetration enhancer-containing spanlastics (PECSs) for transdermal delivery of haloperidol: in vitro characterization, ex vivo permeation and in vivo biodistribution studies. Drug Deliv. 25, 12–22.
Fatemizadeh, M., Tafvizi, F., Shamsi, F., Amiri, S., Farajzadeh, A., Akbarzadeh, I., 2022. Apoptosis induction, cell cycle arrest and anti-cancer potential of tamoxifen-curcumin loaded niosomes against MCF-7 cancer cells. Iran. J. Pathol. 17, 183.
Guo, Q., Liu, Z., Jiang, L., Liu, M., Ma, J., Yang, C., Han, L., Nan, K., Liang, X., 2016. Metformin inhibits growth of human non-small cell lung cancer cells via liver kinase B-1-independent activation of adenosine monophosphate-activated protein kinase. Mol. Med. Rep. 13, 2590–2596.
Haider, S., Yao, C.Q., Sabine, V.S., Grzadkowski, M., Stimper, V., Starmans, M.H., Wang, J., Nguyen, F., Moon, N.C., Lin, X., 2018. Pathway-based subnetworks enable cross-disease biomarker discovery. Nat. Commun. 9, 4746.
Han, D., Li, S.-J., Zhu, Y.-T., Liu, L., Li, M.-X., 2013. LKB1/AMPK/mTOR signaling pathway in non-small-cell lung cancer. Asian Pac. J. Cancer Prev. 14, 4033–4039.
Hashemzadeh, N., Dolatkhah, M., Adibkia, K., Aghanejad, A., Barzegar-Jalali, M., Omidi, Y., Barar, J., 2021. Recent advances in breast cancer immunotherapy: the promising impact of nanomedicines. Life Sci. 271, 119110.
He, Y., Gan, M., Wang, Y., Huang, T., Wang, J., Han, T., Yu, B., 2021. EGFR-ERK induced activation of GRHL1 promotes cell cycle progression by up-regulating cell cycle related genes in lung cancer. Cell Death Dis. 12, 430.
Heberle, H., Meirelles, G.V., da Silva, F.R., Telles, G.P., Minghim, R., 2015. InteractiVenn: a web-based tool for the analysis of sets through Venn diagrams. BMC Bioinform. 16, 1–7.
Heng, Y., Zhu, X., Wu, Q., Lin, H., Ding, X., Tao, L., Lu, L., 2023. High Expression of Tumor HLA-DR Predicts Better Prognosis and Response to Anti-PD-1 Therapy in Laryngeal Squamous Cell Carcinoma. Transl. Oncol. 33, 101678.
Hisada, Y., Yasunaga, M., Hanaoka, S., Saijou, S., Sugino, T., Tsuji, A., Saga, T., Tsumoto, K., Manabe, S., Kuroda, J.-I., 2013. Discovery of an uncovered region in fibrin clots and its clinical significance. Sci. Rep. 3, 1–7.
Huynh, T.Y.L., Oscilowska, I., Szoka, L., Piktel, E., Baszanowska, W., Bielawska, K., Bucki, R., Miltyk, W., Palka, J., 2022. Metformin induces PRODH/POX-dependent apoptosis in breast cancer cells. Front. Mol. Biosci. 465.
Ibáñez, L., Jaramillo, A.M., Ferrer, A., de Zegher, F., 2005. High neutrophil count in girls and women with hyperinsulinaemic hyperandrogenism: normalization with metformin and flutamide overcomes the aggravation by oral contraception. Hum. Reprod. 20, 2457–2462.
Idell, S., Pueblitz, S., Emri, S., Gungen, Y., Gray, L., Kumar, A., Holiday, D., Koenig, K.B., Johnson, A.R., 1995. Regulation of fibrin deposition by malignant mesothelioma. Am. J. Pathol. 147, 1318.
Im, J.H., Fu, W., Wang, H., Bhatia, S.K., Hammer, D.A., Kowalska, M.A., Muschel, R.J., 2004. Coagulation facilitates tumor cell spreading in the pulmonary vasculature during early metastatic colony formation. Cancer Res. 64, 8613–8619.
Ismail, I.S., Amodu, A.D., 2016. Carbonic anhydrase: a new therapeutic target for managing diabetes. J. Metab. Syndr. 5, 1000196.
Iyama, T., Abolhassani, N., Tsuchimoto, D., Nonaka, M., Nakabeppu, Y., 2010. NUDT16 is a (deoxy) inosine diphosphatase, and its deficiency induces accumulation of single-strand breaks in nuclear DNA and growth arrest. Nucleic Acids Res. 38, 4834–4843.
Jaillon, S., Ponzetta, A., Di Mitri, D., Santoni, A., Bonecchi, R., Mantovani, A., 2020. Neutrophil diversity and plasticity in tumour progression and therapy. Nat. Rev. Cancer 20, 485–503.
Jang, S.Y., Kim, A., Kim, J.K., Kim, C., Cho, Y.-H., Kim, J.-H., Kim, C.H., Lee, J.-Y., 2014. Metformin inhibits tumor cell migration via down-regulation of MMP9 in tamoxifen-resistant breast cancer cells. Anticancer Res. 34, 4127–4134.
Johnson, D.E., Burtness, B., Leemans, C.R., Lui, V.W.Y., Bauman, J.E., Grandis, J.R., 2020. Head and neck squamous cell carcinoma. Nat. Rev. Dis. Primers. 6, 92.
Kanaani, L., Ebrahimifar, M., Khiyavi, A.A., Mehrdiba, T., 2017. Effects of cisplatin-loaded niosomal nanoparticleson BT-20 human breast carcinoma cells. Asian Pacific J. Cancer Prev. 18, 365.
Kao, P.Y., Leung, K.H., Chan, L.W., Yip, S.P., Yap, M.K., 2017. Pathway analysis of complex diseases for GWAS, extending to consider rare variants, multi-omics and interactions. Biochimica et Biophysica Acta (BBA)-General Subjects 1861, 335–353.
Ke, R., Xu, Q., Li, C., Luo, L., Huang, D., 2018. Mechanisms of AMPK in the maintenance of ATP balance during energy metabolism. Cell Biol. Int. 42, 384–392.
Kobayashi, M., Kato, K., Iwama, H., Fujihara, S., Nishiyama, N., Mimura, S., Toyota, Y., Nomura, T., Nomura, K., Tani, J., 2013. Antitumor effect of metformin in esophageal cancer: in vitro study. Int. J. Oncol. 42, 517–524.
Krishan, S., Richardson, D.R., Sahni, S., 2015. Adenosine monophosphate–activated kinase and its key role in catabolism: structure, regulation, biological activity, and pharmacological activation. Mol. Pharmacol. 87, 363–377.
Kumar, C.S., Raja, M., Sundar, D.S., Antoniraj, M.G., Ruckmani, K., 2015. Hyaluronic acid co-functionalized gold nanoparticle complex for the targeted delivery of metformin in the treatment of liver cancer (HepG2 cells). Carbohydr. Polym. 128, 63–74.
Levi, M., van der Poll, T., Büller, H.R., 2004. Bidirectional relation between inflammation and coagulation. Circulation 109, 2698–2704.
Matsumura, Y., Kimura, M., Yamamoto, T., Maeda, H., 1988. Involvement of the kinin-generating cascade in enhanced vascular permeability in tumor tissue. Jpn. J. Cancer Res. 79, 1327–1334.
Mazyed, E.A., Helal, D.A., Elkhoudary, M.M., Abd Elhameed, A.G., Yasser, M., 2021. Formulation and optimization of nanospanlastics for improving the bioavailability of green tea epigallocatechin gallate. Pharmaceuticals 14, 68.
Mazzarino, L., Loch-Neckel, G., dos Santos Bubniak, L., Ourique, F., Otsuka, I., Halila, S., Curi Pedrosa, R., Santos-Silva, M.C., Lemos-Senna, E., Curti Muniz, E., 2015. Nanoparticles made from xyloglucan-block-polycaprolactone copolymers: safety assessment for drug delivery. Toxicol. Sci. 147, 104–115.
Mboge, M.Y., Mahon, B.P., McKenna, R., Frost, S.C., 2018. Carbonic anhydrases: role in pH control and cancer. Metabolites 8, 19.
Mehanna, M.M., Sarieddine, R., Alwattar, J.K., Chouaib, R., Gali-Muhtasib, H., 2020. Anticancer activity of thymoquinone cubic phase nanoparticles against human breast cancer: formulation, cytotoxicity and subcellular localization. Int. J. Nanomedicine 9557–9570.
Mekkawy, A.I., Eleraky, N.E., Soliman, G.M., Elnaggar, M.G., Elnaggar, M.G., 2022. Combinatorial therapy of Letrozole-and Quercetin-loaded spanlastics for enhanced cytotoxicity against MCF-7 breast cancer cells. Pharmaceutics 14, 1727.
Meng, S., 2014. The anticancer effect of metformin, the most commonly used anti-diabetes drug. J. Endocrinol. Diab. Obes 2, 1030–1035.
Missale, F., Bugatti, M., Marchi, F., Mandelli, G.E., Bruni, M., Palmerini, G., Monti, M., Bozzola, A.M., Arena, G., Guastini, L., 2023. The prometastatic relevance of tumor-infiltrating B lymphocytes in laryngeal squamous cell carcinoma. Clin. Transl. Immunol. 12, e1445.
Mokale, V., Rajput, R., Patil, J., Yadava, S., Naik, J., 2016. Formulation of metformin hydrochloride nanoparticles by using spray drying technique and in vitro evaluation of sustained release with 32-level factorial design approach. Dry. Technol. 34, 1455–1461.
Mollinedo, F., 2019. Neutrophil degranulation, plasticity, and cancer metastasis. Trends Immunol. 40, 228–242.
Morse, M.A., Sun, W., Kim, R., He, A.R., Abada, P.B., Mynderse, M., Finn, R.S., 2019. The role of Angiogenesis in Hepatocellular CarcinomaRole of Angiogenesis in HCC. Clin. Cancer Res. 25, 912–920.
Mullen, N.J., Singh, P.K., 2023. Nucleotide metabolism: a pan-cancer metabolic dependency. Nat. Rev. Cancer 1–20.
Mynhardt, C., Damelin, L.H., Jivan, R., Peres, J., Prince, S., Veale, R.B., Mavri-Damelin, D., 2018. Metformin-induced alterations in nucleotide metabolism cause 5-fluorouracil resistance but gemcitabine susceptibility in oesophageal squamous cell carcinoma. J. Cell. Biochem. 119, 1193–1203.
Nagy, J.A., Dvorak, A.M., Dvorak, H.F., 2012. Vascular hyperpermeability, angiogenesis, and stroma generation. Cold Spring Harb. Perspect. Med. 2, a006544.
Nitori, N., Ino, Y., Nakanishi, Y., Yamada, T., Honda, K., Yanagihara, K., Kosuge, T., Kanai, Y., Kitajima, M., Hirohashi, S., 2005. Prognostic significance of tissue factor in pancreatic ductal adenocarcinoma. Clin. Cancer Res. 11, 2531–2539.
Osama, H., Sayed, O.M., Hussein, R.R., Abdelrahim, M., Elberry, A., 2020. Design, optimization, characterization, and in vivo evaluation of sterosomes as a carrier of metformin for treatment of lung cancer. J. Liposome Res. 30, 150–162.
Park, D.W., Jiang, S., Tadie, J.-M., Stigler, W.S., Gao, Y., Deshane, J., Abraham, E., Zmijewski, J.W., 2013. Activation of AMPK enhances neutrophil chemotaxis and bacterial killing. Mol. Med. 19, 387–398.
Pastorekova, S., Gillies, R.J., 2019. The role of carbonic anhydrase IX in cancer development: links to hypoxia, acidosis, and beyond. Cancer Metastasis Rev. 38, 65–77.
Pushpakom, S., Iorio, F., Eyers, P.A., Escott, K.J., Hopper, S., Wells, A., Doig, A., Guilliams, T., Latimer, J., McNamee, C., 2019. Drug repurposing: progress, challenges and recommendations. Nat. Rev. Drug Discov. 18, 41–58.
Queiroz, E.A., Puukila, S., Eichler, R., Sampaio, S.C., Forsyth, H.L., Lees, S.J., Barbosa, A. M., Dekker, R.F., Fortes, Z.B., Khaper, N., 2014. Metformin induces apoptosis and cell cycle arrest mediated by oxidative stress, AMPK and FOXO3a in MCF-7 breast cancer cells. PLoS One 9, e98207.
Rego, D.F., Elias, S.T., Amato, A.A., De Luca Canto, G., Guerra, E.N.S., 2017. Anti-tumor effects of metformin on head and neck carcinoma cell lines: a systematic review. Oncol. Lett. 13, 554–566.
Rena, G., Hardie, D.G., Pearson, E.R., 2017. The mechanisms of action of metformin. Diabetologia 60, 1577–1585.
Rezuchova, I., Bartosova, M., Belvoncikova, P., Takacova, M., Zatovicova, M., Jelenska, L., Csaderova, L., Meciarova, I., Pohlodek, K., 2023. Carbonic Anhydrase IX in Tumor Tissue and Plasma of breast cancer patients: reliable biomarker of Hypoxia and Prognosis. Int. J. Mol. Sci. 24, 4325.
Saber, S., Raafat, S., Elashiry, M., El-Banna, A., Schäfer, E., 2023. Effect of different sealers on the cytocompatibility and osteogenic potential of human periodontal ligament stem cells: an in vitro study. J. Clin. Med. 12, 2344.
Salani, B., Maffioli, S., Hamoudane, M., Parodi, A., Ravera, S., Passalacqua, M., Alama, A., Nhiri, M., Cordera, R., Maggi, D., 2012. Caveolin-1 is essential for metformin inhibitory effect on IGF1 action in non-small-cell lung cancer cells. FASEB J. 26, 788–798.
Salem, H.F., Nafady, M.M., Ali, A.A., Khalil, N.M., Elsisi, A.A., 2022. Evaluation of metformin hydrochloride tailoring bilosomes as an effective transdermal nanocarrier. Int. J. Nanomedicine 1185–1201.

Sanchez-Rangel, E., Inzucchi, S.E., 2017. Metformin: clinical use in type 2 diabetes. Diabetologia 60, 1586–1593.
Saraei, P., Asadi, I., Kakar, M.A., Moradi-Kor, N., 2019. The beneficial effects of metformin on cancer prevention and therapy: a comprehensive review of recent advances. Cancer Manag. Res. 11, 3295.
Schiliro, C., Firestein, B.L., 2021. Mechanisms of metabolic reprogramming in cancer cells supporting enhanced growth and proliferation. Cells 10, 1056.
Seto, S.I., Onodera, H., Kaido, T., Yoshikawa, A., Ishigami, S.I., Arii, S., Imamura, M., 2000. Tissue factor expression in human colorectal carcinoma: correlation with hepatic metastasis and impact on prognosis. Cancer Interdiscipl. Int. J. Am. Cancer Soc. 88, 295–301.
Shaaban, M., Nasr, M., Tawfik, A.A., Fadel, M., Sammour, O., 2019. Novel bergamot oil nanospanlastics combined with PUVB therapy as a clinically translatable approach for vitiligo treatment. Drug Deliv. Transl. Res. 9, 1106–1116.
Shaker, D.S., Shaker, M.A., Hanafy, M.S., 2015. Cellular uptake, cytotoxicity and in-vivo evaluation of Tamoxifen citrate loaded niosomes. Int. J. Pharm. 493, 285–294.
Shamma, R.N., Sayed, S., Sabry, N.A., El-Samanoudy, S.I., 2019. Enhanced skin targeting of retinoic acid spanlastics: in vitro characterization and clinical evaluation in acne patients. J. Liposome Res. 29, 283–290.
Shannon, P., Markiel, A., Ozier, O., Baliga, N.S., Wang, J.T., Ramage, D., Amin, N., Schwikowski, B., Ideker, T., 2003. Cytoscape: a software environment for integrated models of biomolecular interaction networks. Genome Res. 13, 2498–2504.
Sharma, A., Pahwa, S., Bhati, S., Kudeshia, P., 2020. Spanlastics: a modern approach for nanovesicular drug delivery system. Int. J. Pharm. Sci. Res. 11, 1057–1065.
Shatova, O., Butenko, E.V., Khomutov, E.V., Kaplun, D., Sedakov, I.E., Zinkovych, I., 2016. Metformin impact on purine metabolism in breast cancer. Biomed. Khim. 62, 302–305.
Shoji, M., Hancock, W.W., Abe, K., Micko, C., Casper, K.A., Baine, R.M., Wilcox, J.N., Danave, I., Dillehay, D.L., Matthews, E., 1998. Activation of coagulation and angiogenesis in cancer: immunohistochemical localization in situ of clotting proteins and vascular endothelial growth factor in human cancer. Am. J. Pathol. 152, 399.
Shukla, S.K., Kulkarni, N.S., Chan, A., Parvathaneni, V., Farrales, P., Muth, A., Gupta, V., 2019. Metformin-encapsulated liposome delivery system: an effective treatment approach against breast cancer. Pharmaceutics 11, 559.
Silvain, J., Collet, J.-P., Nagaswami, C., Beygui, F., Edmondson, K.E., Bellemain-Appaix, A., Cayla, G., Pena, A., Brugier, D., Barthelemy, O., 2011. Composition of coronary thrombus in acute myocardial infarction. J. Am. Coll. Cardiol. 57, 1359–1367.
Skaf, E., Stein, P.D., Beemath, A., Sanchez, J., Bustamante, M.A., Olson, R.E., 2005. Venous thromboembolism in patients with ischemic and hemorrhagic stroke. Am. J. Cardiol. 96, 1731–1733.
Standeven, K.F., Ariëns, R.A., Whitaker, P., Ashcroft, A.E., Weisel, J.W., Grant, P.J., 2002. The effect of dimethylbiguanide on thrombin activity, FXIII activation, fibrin polymerization, and fibrin clot formation. Diabetes 51, 189–197.
Tawfik, S.M., Abdollah, M.R., Elmazar, M.M., El-Fawal, H.A., Abdelnaser, A., 2022. Effects of metformin combined with antifolates on HepG2 cell metabolism and cellular proliferation. Front. Oncol. 12, 164.
Teaima, M.H., El Mohamady, A.M., El-Nabarawi, M.A., Mohamed, A.I., 2020. Formulation and evaluation of niosomal vesicles containing ondansetron HCL for trans-mucosal nasal drug delivery. Drug Dev. Ind. Pharm. 46, 751–761.
Turashvili, G., Leung, S., Turbin, D., Montgomery, K., Gilks, B., West, R., Carrier, M., Huntsman, D., Aparicio, S., 2009. Inter-observer reproducibility of HER2 immunohistochemical assessment and concordance with fluorescent in situ hybridization (FISH): pathologist assessment compared to quantitative image analysis. BMC Cancer 9, 1–13.
Ueno, T., Toi, M., Koike, M., Nakamura, S., Tominaga, T., 2000. Tissue factor expression in breast cancer tissues: its correlation with prognosis and plasma concentration. Br. J. Cancer 83, 164–170.
Ugwueze, C.V., Ogamba, O.J., Young, E.E., Onyenekwe, B.M., Ezeokpo, B.C., 2020. Metformin: a possible option in cancer chemotherapy. Anal. Cell. Pathol. 2020.
Vahidfar, N., Aghanejad, A., Ahmadzadehfar, H., Farzanehfar, S., Eppard, E., 2021. Theranostic advances in breast cancer in nuclear medicine. Int. J. Mol. Sci. 22, 4597.
van den Berg, Y.W., Osanto, S., Reitsma, P.H., Versteeg, H.H., 2012. The relationship between tissue factor and cancer progression: insights from bench and bedside. Blood J. Am. Soc. Hematol. 119, 924–932.
Van Opdenbosch, N., Lamkanfi, M., 2019. Caspases in cell death, inflammation, and disease. Immunity 50, 1352–1364.
Wang, J., Gao, Q., Wang, D., Wang, Z., Hu, C., 2015. Metformin inhibits growth of lung adenocarcinoma cells by inducing apoptosis via the mitochondria-mediated pathway. Oncol. Lett. 10, 1343–1349.
Wang, Y., Wan, F., Chang, K., Lu, X., Dai, B., Ye, D., 2017. NUDT expression is predictive of prognosis in patients with clear cell renal cell carcinoma. Oncol. Lett. 14, 6121–6128.
Wang, J.-J., Liu, T.-H., Li, J., Li, D.-N., Tian, X.-Y., Ouyang, Q.-G., Cai, J.-P., 2020. The high expression of MTH1 and NUDT5 predict a poor survival and are associated with malignancy of esophageal squamous cell carcinoma. PeerJ 8, e9195.
Wang, W., Cui, J., Ma, H., Lu, W., Huang, J., 2021a. Targeting pyrimidine metabolism in the era of precision cancer medicine. Front. Oncol. 11, 684961.
Wang, Y., Zhang, Y., Feng, X., Tian, H., Fu, X., Gu, W., Wen, Y., 2021b. Metformin inhibits mTOR and c-Myc by decreasing YAP protein expression in OSCC cells. Oncol. Rep. 45, 1249–1260.
Witkowski, M., Friebel, J., Tabaraie, T., Grabitz, S., Dörner, A., Taghipour, L., Jakobs, K., Stratmann, B., Tschoepe, D., Landmesser, U., 2021. Metformin is associated with reduced tissue factor procoagulant activity in patients with poorly controlled diabetes. Cardiovasc. Drugs Ther. 35, 809–813.
Wright, R.H., Beato, M., 2021. Role of the NUDT enzymes in breast cancer. Int. J. Mol. Sci. 22, 2267.
Xin, G., Wei, Z., Ji, C., Zheng, H., Gu, J., Ma, L., Huang, W., Morris-Natschke, S.L., Yeh, J.-L., Zhang, R., 2016. Metformin uniquely prevents thrombosis by inhibiting platelet activation and mtDNA release. Sci. Rep. 6, 36222.
Yenmiş, G., Beşli, N., Sarac, E.Y., Emre, F.S.H., Şenol, K., KanigÜr, G., 2021. Metformin promotes apoptosis in primary breast cancer cells by downregulation ofcyclin D1 and upregulation of P53 through an AMPK-alpha independent mechanism. Turkish J. Med. Sci. 51, 826–834.
Yin, J., Ren, W., Huang, X., Deng, J., Li, T., Yin, Y., 2018. Potential mechanisms connecting purine metabolism and cancer therapy. Front. Immunol. 9, 1697.
Yu, H., Zhong, X., Gao, P., Shi, J., Wu, Z., Guo, Z., Wang, Z., Song, Y., 2019. The potential effect of metformin on cancer: an umbrella review. Front. Endocrinol. (Lausanne) 10, 617.
Zhao, W., Chen, C., Zhou, J., Chen, X., Cai, K., Shen, M., Chen, X., Jiang, L., Wang, G., 2022. Inhibition of autophagy promotes the anti-tumor effect of metformin in oral squamous cell carcinoma. Cancers (Basel) 14, 4185.